POLITECNICO
MILANO 1863

SCUOLA DI INGEGNERIA INDUSTRIALE
E DELL'INFORMAZIONE

Numerical Investigation of the Aerodynamic Interference Effects for a Coaxial Rotor Configuration

Tesi di Laurea Magistrale in
Aeronautical Engineering - Ingegneria Aeronautica

Author: **Clara Rondeau Gómez**

Student ID: 984910
Advisor: Prof. Luigi Vigevano
Academic Year: 2022-23

Abstract

In recent years, the aeronautical industry has embraced the eVTOL concept (electrical Vertical Take-Off and Landing vehicles) to provide more intelligent, eco-friendly, well-integrated, and sustainable mobility options. The novel idea has emerged in response to the recent increasing number of large metropolitan areas with high populations. The key features of this concept include the use of electrical power, and the incorporation of multi-propellers. One particular challenge arises from the usage of several propellers nearby: understanding the flow interference between rotors. Hence, an aerodynamic investigation is needed to better understand this rotor-rotor interaction, alongside data gathering for a future noise prediction computation.

This investigation is focused on the numerical modelling of a coaxial rotor configuration in hover conditions, with the use of the in-house ROSITA software, a high-fidelity CFD code specialized in rotor aerodynamics. To have a wider understanding of the rotor-rotor interaction, the study of the isolated rotor is crucial. For this reason, two different configurations, isolated and coaxial, have been put in comparison, where their rotor wakes, induced velocity fields, aerodynamic loads, vorticity, etc. have been analyzed. Additionally, data from the Aeronautical Research and Technology in Europe (GARTEUR) group, more precisely, the Action Group HC/AG-26, has been used to ratify the validity of the ROSITA's computational results.

The overall evaluation of the results indicates a significant loss in performance of the lower rotor for the coaxial configuration. Yet, a solid match of the data verifies the reliability of the employed model when simulation the aerodynamics of isolated and coaxial rotors.

Keywords: eVTOL, Rotor-rotor interference, Aerodynamics, CFD, ROSITA

Sommario

Negli ultimi anni, l'industria aeronautica ha abbracciato il concetto di eVTOL (veicoli elettrici a decollo e atterraggio verticale) per fornire opzioni di mobilità più intelligenti, eco-compatibili, ben integrate e sostenibili. Questa idea innovativa è emersa in risposta al recente aumento del numero di grandi aree metropolitane ad alta densità di popolazione. Le caratteristiche principali di questo concetto sono l'uso dell'energia elettrica e l'incorporazione di multi-rotori. Una sfida particolare deriva dall'utilizzo di più rotori posti a distanza ravvicinata vicine: la comprensione delle interferenze di flusso tra i rotori. Pertanto, è necessaria un'indagine aerodinamica per comprendere meglio le interazioni rotore-rotore, oltre alla raccolta di dati per un futuro calcolo di previsione del rumore.

Questa indagine si concentra sulla modellazione numerica di una configurazione di rotori coassiali in condizioni di hovering, con l'uso del software ROSITA, un codice CFD ad alta fedeltà specializzato nell'aerodinamica dei rotori. Per avere una più ampia comprensione dell'interazione rotore-rotore, lo studio del rotore isolato è fondamentale. Per questo motivo, due diverse configurazioni, isolate e coassiali, sono state messe a confronto, analizzando le loro scie, i campi di velocità indotti, i carichi aerodinamici, campi di vorticità, ecc. Inoltre, i dati ottenuti dal gruppo Ricerca e Tecnologia Aeronautica in Europa (GARTEUR), più precisamente dal Gruppo d'Azione HC/AG-26, sono stati utilizzati per ratificare la validità dei risultati di calcolo di ROSITA.

La valutazione complessiva dei risultati ottenuti indica una significativa perdita di prestazioni del rotore inferiore per la configurazione coassiale. La significativa corrispondenza tra dati sperimentali e calcolati verifica l'affidabilità del modello impiegato nella simulazione dell'aerodinamica di rotori isolati e coassiali.

Parole chiave: eVTOL, Interferenza rotore-rotore , Aerodinamica, CFD, ROSITA

Contents

1 | Introduction

1.1. Background & Motivation

This last decade, there's been an exponential growth in population in cities around the world, making urban mobility one of the main issues to solve, or at least, improve the way people get from one place to another without wasting hours due to road traffic. There have been many ideas and proposals for this topic, such as creating new mobility infrastructures (roads, highways...), promoting the usage of public transport, or the innovative concept called *Urban Air Mobility* [20].
This last concept refers to an emerging topic in the field of transport that seeks to use aircraft, such as UAVs, for the movement of people and goods within the urban environment, and provide more efficient, faster, and sustainable mobility solutions in congested urban areas. The potential applications for the *Urban Air Mobility* apart from the transportation of people and delivery of goods, also covers the rescue and emergency services, for example. It is worth mentioning that, despite the promising possibilities, this new concept faces significant challenges, such as airspace regulation, safety, integration with existing infrastructure, and public acceptance. However, several companies and industries, including technology and aviation, are investing in the development of technologies and solutions to accomplish this vision of urban air mobility.

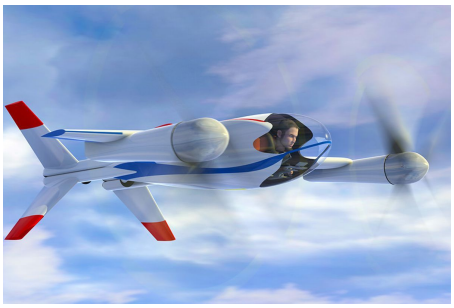

Figure 1.1: NASA Puffin [17]

Thanks to recent investigations and technological developments, it has been proven that Vertical Takeoff and Landing (VTOL) vehicles are fundamental for the implementation of the UAM concept, which its ability to take off and land vertically is crucial for limited urban environments. However, these vehicles come with drawbacks; for instance, helicopters are excessively expensive, polluting, and noisy, making them impractical for operating in urban environments with high demand. Therefore, the feasibility of using electrical VTOLs (eVTOLs) [18] has been and remains the focus of recent studies. This new

concept raised in popularity in 2010 when the NASA Puffin paper was published [17], showing a single-person concept rendering of the technology during the flight, Figure 1.1, where NASA developed a new technology called Distributed Electric Propulsion (DEP). Consequently, many aircraft manufacturers such as Boeing [11], Airbus [16], and Bell [21] have raised interest concerning eVTOLs, and even, developing new prototypes, Figure 1.2.

(a) Airbus A3 Vahana [16]

(b) Boeing-Aurora Flight Sciences PAV [11]

Figure 1.2: eVTOLs configurations comparison

Thanks to the motivation of these big companies, startups and academia have played a crucial role in advancing the development of these air vehicles and, have occasionally taken the lead in technological advancements.
Having a look into the design field, eVTOL vehicles typically feature numerous small propulsion units powered by electric motors (DEP) [23]. The ability to position these propulsion units almost anywhere results in a wide range of configurations, highlighting the essential need for a performance evaluation strategy capable of handling diverse layouts. The most frequent configuration is the use of multiple propellers, as shown in Figures 1.2, where they can present certain regions of overlapping between the rotor disks, being the side-by-side and tandem configurations the most common ones. In particular, from an aerodynamic perspective, the interaction between rotors stands out as a meaningful phenomenon that defines the airflow around the majority of eVTOLs, influencing their performance, characteristics, and noise levels. Hence, understanding this behaviour (rotor-rotor interaction) is crucial to optimize the aircraft and its performance.

The present investigation will focus on the multi-rotor configuration, more precisely on the coaxial one.

1.2. Literature review

Even with the rapidly advancing of computational fluid dynamics (CFD) techniques, accurately calculating the aerodynamic performance of coaxial rotors remains a challenging task. Hence, performing experimental tests is a crucial method to study the aerodynamics of coaxial rotors for a future comparison with computational results.

This thesis is based on the data and results obtained in [24], in order to add information and to have a wider vision and knowledge of the mentioned research.

The group of Aeronautical Research and Technology in Europe (GARTEUR) followed a series of activities in collaboration with 14 different universities and research centres (Action Group HC/AG-26) coordinated by DLR to study the acoustic and aerodynamic characteristics of small rotor configurations, including the already mentioned rotor-rotor interactions. Some of the many research centres that helped to develop the project were Politecnico di Milano, the German Aerospace Center - DLR, the Italian Aerospace Research Center - CIRA, the French Aerospace Center - ONERA, and the University of Glasgow, among others. The study aimed to compare numerical activities with wing tunnel testings on a small rotor provided by DLR, (Figure 3.2). The experimental and simulation tests played with different placements of the rotor, including the isolated, tandem, and coaxial configurations. The wind tunnel experiments for aeroacoustics were done in DLR's Acoustic Wind Tunnel Braunschweig (AWB) [19]. Each group used a different numerical method for the aerodynamic simulations, varying from lifting line to CFD, to compare test data and code validations. Thanks to the wind tunnel data, some of the partners were able to validate the database of the different numerical methods used and also, in return, to ratify the experimental veracity by reproducing the same experiments in different wind tunnels. Tables 1.1 & 1.2, taken from [24] provide a summary of the numerical methodologies employed within the GARTEUR Action Group HC/AG-26.

Partner	Grid Cells ISO/Multi (Million)	Time step ISO/Multi	Num. of revs ISO/Multi
DLR - TAU	34.2	stationary	stationary
IAG - FLOWer	14.3/24	$0.5^{o}/0.5^{o}$	25/25
Polimi - SU2	30	$1^{o}/1^{o}$	20/20
UoG	18.3	$1^{o}/2^{o}$	10/10

Table 1.1: Summary of CFD grids used by the partners

Partner	Code	Desciption
CIRA	RAMSYS, ACO-suite	Unsteady, inviscid and incompressible, Boundary Element Method (BEM),Ffowcs Williams/Hawkings (FW-H), freewake
DLR	UPM, TAU, APSIM	Free Wake Panel, method, unstructured, CFD, FW-H
ONERA	PUMA, KIM	Unsteady lifting line / free-wake solver, FW-H
Polimi	DUST, SU2	Free Wake Panel method and unsteady, compressible (URANS) CFD, FW-H
Uni Stuttgart	FLOWer, ACCO	Flower: unsteady, compressible (URANS) CFD solver with Chimera technique, FW-H Solver with source-time
RomaTre University	RM3	Free wake boundary element method (BEM) + FWH
UoG	HMB3-HFWH	HM3 CFD solver, FW-H coupled with HMB3

Table 1.2: Codes' characteristics used by the partners

Further in this research, Table 1.1 will be very valuable in order to compare ROSITA's simulations and their characteristics with the ones done previously.

Some other articles and papers have been reviewed to have a broader view of the complex aerodynamic characteristics of coaxial hovering rotors.

In the early years, Harrington [10] performed an aerodynamic test on a hovering coaxial helicopter rotor and compared it against a single isolated rotor by measuring its static thrust and torque performance over a range of airspeeds. While Coleman [6] provided a summary of the initial experimental findings on the aerodynamic efficiency of coaxial configuration and its applications. The main issues that Coleman addressed were the rotor separation distance, their wake structure, swirl recovery, and the effects of having no tail rotor.

Apart from the experimental testing, numerical calculations are also crucial for studying the aerodynamic performance, and even better, if both methodologies, experimental and computational, are being compared. The well-known CFD techniques are capable of representing the complex structure of propellers. Lakshminarayan [13], for example, used the sliding and overset technique to study the interference and dynamic behaviour of vortex-vortex and blade-vortex interactions of a conventional hovering coaxial rotor.

Additionally, again for the coaxial configuration, Brown and Kim [2] developed an analytical approach using the viscous vortex transport model to calculate the profile, induced, and parasite contributions to the overall power consumed by the coaxial and isolated configurations. The main conclusion of this study was that the coaxial system in hovering conditions required less induced power than a conventional one (conventional meaning that it has the same overall solidity, number of blades, and blades' aerodynamic properties). The reason behind the reduction of induced power is the change in performance of the upper rotor. The convection rate of the vortices from the upper rotor is increased because they pass through the lower rotor downwash region, so, the tip vortices created by the upper rotor move faster than those generated by the lower rotor. Hence, the total axial descent rate of the tip vortices is increased compared to the rate at which the vortices would convect as if the rotors were to be operated alone. Due to this faster convection, the blade-wake interaction weakens, reducing the power consumption on the outer parts of the upper rotor.

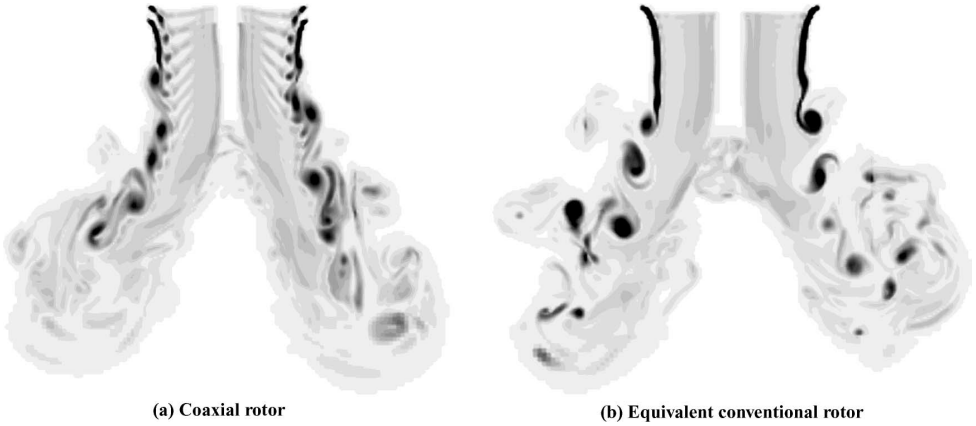

Figure 1.3: Wake structure in hover from [2]

Figure 1.3 taken from [2] reaffirms the statement of a reduction of induced power, by showing the wake flowfield near the rotors for both coaxial and conventional rotors. In both cases, the wake is deformed because the small tip swirls turn into bigger swirls. However, for the coaxial case both tip vortices, from upper and lower rotors, merge creating a larger single sequence of vortical structure. This behaviour is well explained by Landgrebe [14], in which he found, by studying the wake shape of hovering rotors, that when these big vortical structures start to form and convect downstream, the wake starts to expand in diameter, hence, there is no more wake contraction. As a result of their mutual interaction, these structures eventually get self-destroyed, forming the large-scale, highly disordered, low-level vorticity field visible in the far-wake of both images.

Another interesting investigation was done by J. Deng [8], where wind tunnel tests, and numerical computations were done to study the aerodynamic characteristics of a rigid coaxial rotor in hover and forward flight. When assessing the research results, the main feature of the hovering coaxial configuration is the reduction of thrust for the lower rotor due to a decrease in the effective angle of attack caused by the upper rotor downwash. Keeping with the wake structure analysis done by Landgrebe [14], J. Deng compares the induced velocity field for the coaxial and single rotor obtained using CFD. Figure 1.4 shows that the wake contraction rate of the coaxial rotor is smaller than the single one due to the already-mentioned effect caused by the big vortical structures convected downstream.

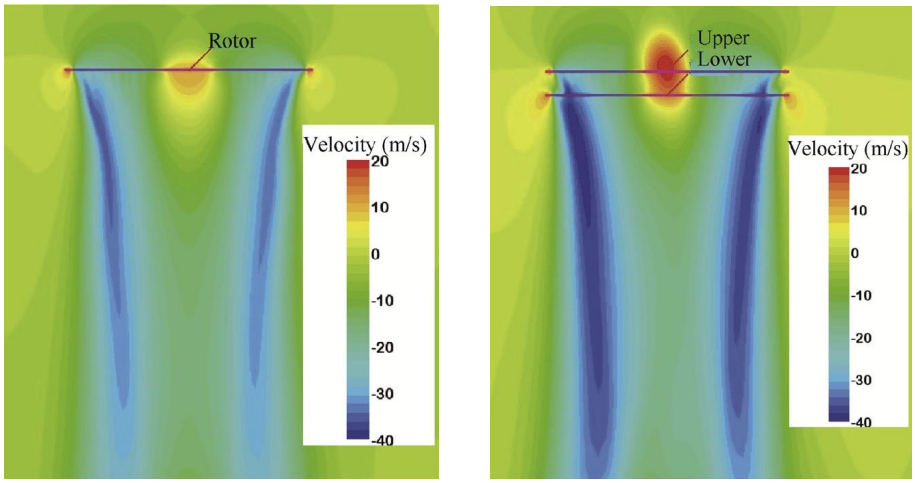

(a) Single rotor (b) Coaxial rotor

Figure 1.4: Induced velocity field comparison from [8]

Another valuable analysis from Deng's investigation, that further in this research will appear, is the aerodynamic loads interference between the two rotors.

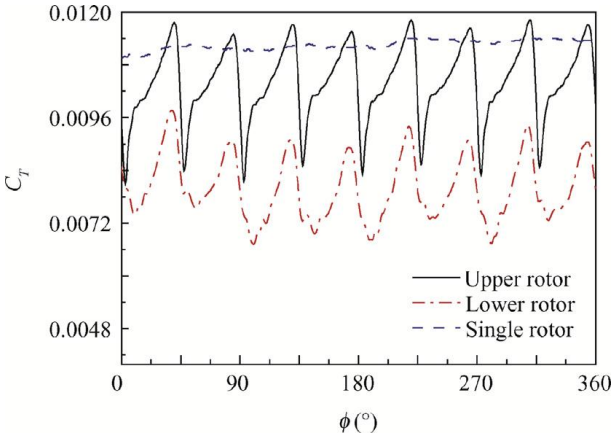

Figure 1.5: Thrust coefficient for upper and lower rotors in calulations [8]

Figure 1.5 shows the variation of thrust coefficient throughout one revolution. As Deng's rotor has 4 blades, the upper and lower propellers meet each other at every 45º, hence, eight times per cycle. This translates to the eight periodic changes in the rotors' thrust. When two blades from the upper and lower rotors are about to overlap, the bound vortices of one blade causes an upwash on the other blade, increasing thrust. When the two blades rotate away from one another, the upwash becomes downwash and then, the thrust reduces.

In short, a great amount of data has been found for the hovering coaxial rotors' configuration that will help to prove the validity of the obtained results and validate the efficiency and accuracy of the ROSITA's code.

1.3. Objective of the work

The main goal of this research is to provide valuable information to the eVTOL UAM field by means of a numerical aerodynamics investigation of the interference effects of a coaxial rotor configuration in hover conditions. The numerical study will be done with a CFD code developed by Politecnico di Milano named ROSITA. It is a high-fidelity CFD code specialized in rotor aerodynamics, which its main features are the usage of multi-block structured grids, a Chimera method, and RANS equations. To better understand this rotor-rotor interaction, besides the computation of the coaxial configuration, the performance of an isolated rotor will be also analysed and put in comparison. The differences between their rotor wakes, induced velocity fields, aerodynamic loads, vorticities, etc. will be determined to obtain valuable conclusions.

In the context of this work, which is also intended to broaden the knowledge of CFD and

all its implications, two types of simulations, steady and unsteady, will be conducted for the isolated case, where the results of these two setups will be presented in an attempt to comprehend the reason behind those differences, if they exist.

As mentioned, previous numerical studies have been conducted on the coaxial configuration [24], more precisely the already mentioned GARTEUR Action Group HC/AG-26, hence, the validity of the different simulation results is going to be checked.

2 | Rotor Aerodynamics Framework

This chapter aims to outline the simulation framework for aerodynamics, based on the usage of the Navier-Stokes equations. The aerodynamic study is done by using a multi-block structured RANS solver named ROSITA (ROtorcraft Software ITaly), which apart from computing the near-flow around objects, is able to store the result on specific control surfaces for a future acoustic prediction. All information in this chapter is taken from ROSITA's formulation and User Manual [15].

2.1. ROSITA CFD Solver

To study rotorcraft flows that involve unsteady phenomenons, reverse flow regions, blade-vortex interactions, vortex formations, etc. Politecnico di Milano has developed a CFD code to allow the correct modelling of rotor wakes, named ROSITA. To represent the turbulent characteristics of the flow, it employs a combination of RANS equations with the single-equation Spalart-Allmaras turbulence model. As already said, it uses structured multi-block grids to represent the computational domain that can be fixed or in relative motion. As the domain is composed of more than one mesh, to compute the connectivity between the different grids the *Chimera technique* is used. This technique is based on the modified Chesshire and Henshaw algorithm [5].

2.1.1. Governing Equations

A brief description of ROSITA's formulation will be presented in this section. As mentioned, the code solves the non-dimensional Navier-Stokes equations for a perfect gas in 2D and 3D domains, making use of the SA turbulence model and the proper reference quantities. The different available boundary conditions will also be presented.

- Navier-Stokes equations:
  Considering a 3D viscous flow, the conservative form of the N-S equations is the

following:

$$\begin{cases} \frac{\partial \rho}{\partial t} + \nabla \cdot (\rho u) = 0, \\ \frac{\partial \rho u}{\partial t} + \nabla \cdot (\rho u \otimes u + PI - \mu\tau) = 0, \\ \frac{\partial \rho e^t}{\partial t} + \nabla \cdot (\rho u h^t - \mu\tau \cdot u - K\nabla T) = 0 \end{cases} \tag{2.1}$$

- Non-dimensionalized Eq.:
  The process of non-dimensionalization involves applying a change of variable to every dimensional quantity q_{dim}, which includes space coordinates and time. This transformation results in each adimensional quantity, denoted as q as follows:

$$q = q_r q_{dim} \tag{2.2}$$

  Where q_r is the reference quantity. When using ROSITA, and more precisely when simulating rotorcraft, the employed reference quantities used for the non-dimensionalization are:

  - ρ_∞ : free-stream density
  - c_∞ : free-stream speed of sound
  - l_{ref} : reference length (the rotor radius)

  All of the other values are obtained from the three listed above. Some useful non-dimensional quantities are shown below:

$$\omega = \omega_{dim} \left(\frac{l_{ref}}{c_\infty} \right) \tag{2.3}$$

$$t = t_{dim} \left(\frac{c_\infty}{l_{ref}} \right) \tag{2.4}$$

$$P = \frac{P_{dim}}{(\rho_\infty c_\infty^2)} \tag{2.5}$$

$$F = \frac{F_{dim}}{\left(\rho_\infty c_\infty^2 l_{ref}^2\right)} \tag{2.6}$$

- Boundary Conditions:
  The *Solid Wall B.C.* is characterized by the no-slip condition (zero velocity at the solid boundary), with the need for an additional condition that can be either *adiabatic wall* (zero heat flux) or an *isothermal wall* (imposing wall temperature). The condition for *Velocity Inlet B.C.* is the value of the velocity at infinity: $V_{inlet} = V_\infty$.

For the *Pressure Outlet B.C.*, the value is equal to the infinity one: $P_{outlet} = P_\infty = \frac{1}{\gamma}$. Lastly, there are two more conditions *Farfield B.C.* and *Froude B.C.* If the size of the computational domain is big enough and waves leaving the domain are not reflected, it can be imposed free-stream conditions at the farfield. However, when working with hovering flight, the fluid at the farfield remains at rest (zero velocity), hence, there's the possibility of having a recirculation in the downstream wake region that might extend very close to the rotor disk. A way to avoid this recirculation is to change the free stream velocity outside the computational domain by dividing the grid's outer boundary into inflow and outflow regions. This last condition is called *Froude B.C.* and it is only available for steady simulation in ROSITA.

- Turbulence Modelling:
  As previously noted, ROSITA uses the non-dimensional RANS equations for turbulent compressible flows along with the new reference quantities. The RANS equations employ Boussinesq's eddy viscosity concept, assuming that turbulent stresses are proportionate to the mean velocity gradient, drawing an analogy to viscous stresses in laminar flow, and making this approximation a low-order turbulence model. It is worth mentioning, that when using this software no transition from laminar to turbulent will be considered, hence, the flow will be assumed as fully turbulent.

2.1.2. Numerical Methods

ROSITA uses a spatial discretization of the Navier-Stokes equations that involves using a cell-centered finite-volume implementation of Roe's scheme for structured multi-block meshes. By incorporating the MUSCL extrapolation along a Total Variation Diminishing (TVD) limiter, it can be achieved a high-resolution scheme establishing monotonicity and limiting oscillations in the solutions. Progression in time is accomplished through the usage of a dual-time method.

Chimera Methods

When having complex geometries, it can be hard or almost impossible to create structured grids with smooth properties, hence, to overcome these limitations, a partitioning of the domain into simpler overlapping structured subdomains can be carried out thanks to the *Chimera technique* [5]. It can also be called *Overset Grid Method* [4]. An overset mesh is defined by multiple body-fitted grids that solve the equations around the boundaries, along with a few background grids that cover the remaining part of the domain.

The *Valid Points* are those where the PDE is discretized for each component grid. The *Fringe points* are the ones lying in an overlapping region with another component grid. The solution at these last points (fringe points) is derived through interpolation from the solution at points within the overlapped grid, the resultant points are called *Donor*. Lastly, the points outside the computational domain, for example, the ones that fall inside a solid body, are referred to as *Hole points*. A representation of the different points can be shown in Figure 2.1.

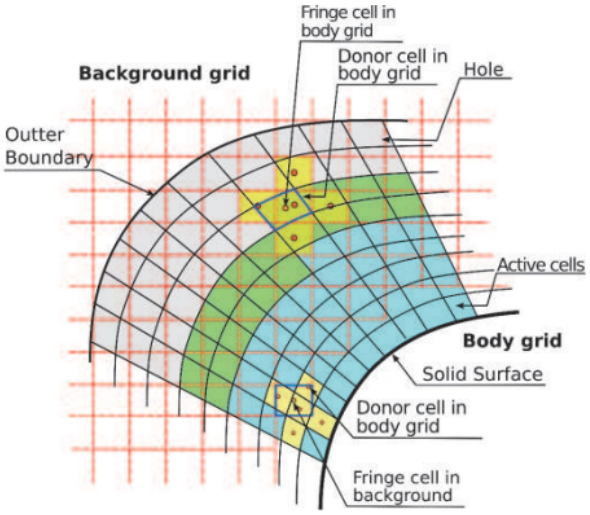

Figure 2.1: Sketch of overset grid

Through the fringe and donor points, the different grids communicate their solution. *Explicit* interpolation, that is the one that ROSITA uses, occurs when a fringe point is restricted from being a donor point simultaneously. In this case, the interpolation involves only valid points with known solutions, from which the flow variables are interpolated. On the contrary, when fringe points serve as donors, the interpolation is called *Implicit*, needing the solution of an equation system to update the fringe points solutions. Although explicit interpolation is simpler to implement, it demands broader overlaps between the different meshes.

For ROSITA to do this explicit interpolation some steps are required: Firstly, an initial identification of the domains where there are solid wall conditions is needed, marking all points in the overlapping meshes near these boundaries as holes (also called *Seed points*). With the use of an iterative algorithm, donor and fringe points can be identified, allowing hole points to extend from the seeds until they completely fill the areas outside the computational domain. For each different mesh, a priority index is assigned during the initial setup, ranging from 1 (lowest priority) to N (highest priority), where N represents the number of different meshes. The overlapping regions will be dominated by the highest priority grids.

Parallelization

The primary objective of parallel programming is to use all accessible processors and reduce the program's elapsed time. To reduce computational time for the simulations, ROSITA offers a parallel version that uses the full capacity of the available processors. As workstation prices have decreased in price, the MPP (Massively Parallel Processors) architecture [1], among others such as SMP or vector computers, experienced growing popularity. A parallel computer using MPP architecture is composed of nodes linked by a high-speed network, with each node having its own processor, memory, and I/O subsystem. It uses distributed processors across the nodes that collaborate to execute a specific task, and in order to access updated data from other processes, must transmit data through the interconnected network. This data transmission is called *message-passing*, where the program is connected to a library responsible for supervising the point-to-point and collective communications among processes.
One of the most common message-passing transmissions, and also used for the parallelization in ROSITA is the so-called Message Passing Interface (MPI) [9]. For ROSITA to do this parallelization, it assigns part of the computational grid to each one of the available processors. The process of dividing the grid in ROSITA consists of three primary steps:

1. Partitioning: involves dividing grid blocks into groups, with the user-defined parameter (`GNPARTS`) setting the number of partitions.

2. Load balancing: involves employing the Wissink-Meakin load balancing algorithm [22], where each grid is assigned a number of processors proportionate to its number of cells.

3. Sub-splitting: each grid block is divided into a number of segments equivalent to the number of processors allocated to it.

The parallel implementation of the flow solver follows a *master/worker* model, where the master process (rank 0) manages tasks such as reading simulation parameters, partitioning the grid, and managing outputs. Instead, the worker process (ranks 1 to N-1) performs the actual computations on their assigned portions of the domain.
The major challenge in the parallel solver is addressing the coupling of solutions at the block boundaries, because the linear system resulting from the discretization of the flow equations is solved independently in each process block, making convergence less straightforward, especially with a large number of processors. Hence, to improve convergence and stability, the Generalized Conjugate Gradient (GCG) method [7] is modified to update connectivity boundary conditions for certain boundaries during each iteration.

3 | Computational Model

The computational setup is going to be discussed in this chapter, beginning with the definition of the geometry, then the generation of the different grid components in order to use the Chimera method, and lastly, a grid independence test to ensure that the results obtained will not dependent on the grids used for the simulations.

3.1. Problem Geometry

To validate the numerical simulations with experimental data, the computational configuration follows the experimental setup outlined in [24]. The experiments are made in the DLR Braunschweig aero-acoustic tunnel (AWB) [19], where the testing room is approximately an 8 m^2 cub size. The anechoic chamber is made of an open-jet Göttingen-type wind tunnel, capable of running at speeds of up to 65 m/s, and optimized for noise measurements at frequencies above 250 Hz. The nozzle is 1.2 m high by 0.8m wide. The rotor blade used is an available commercial rotor blade (Xoar model PJN), more specifically, a two-blade 13x7 rotor, having 13 inches or 0.33m in diameter, Figure 3.2 shows the real dimensions of the rotor blade. Figure 3.1 shows the section profiles along the blade span and the twist (Θ), thickness (t) and cord (c) spanwise. Lastly, for the experimental test in [24], a pylon planform has also been used as a rotor support but not considered in the simulation setup.

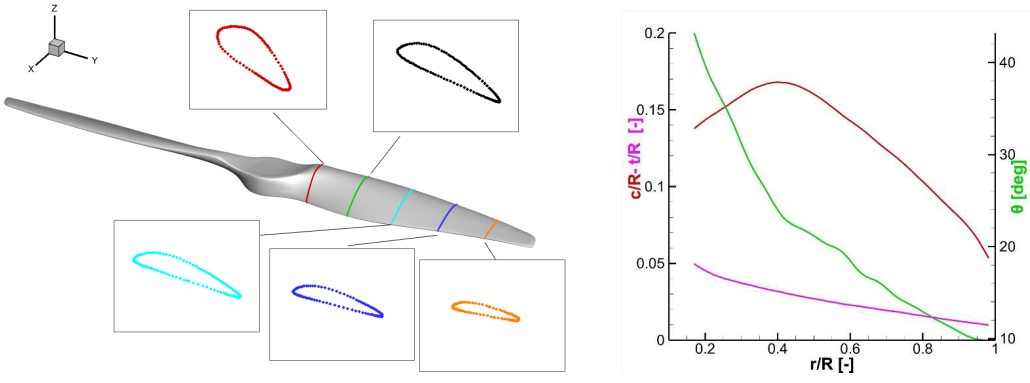

(a) CAD rotor model

(b) Θ, t and c distribution

Figure 3.1: Rotor geometry

For the isolated case, the coordinates' origin lies in the centre of the rotor disk, as shown in Figure 3.2. With this configuration, a single rotor blade is used; but when referring to the coaxial configuration, the Δx and Δy are null (the rotating axis of both rotors are aligned), while the axial distance between the disks is $\Delta z = -0.5R$ (R stands for the radius of the rotor, in this case 0.165 m). In the case of the isolated setup, the rotor is a Right-Handed Rotor (RHR) and spins counterclockwise. For the coaxial case, the lower rotor remains a right-handed rotor, consistent with the isolated configuration. However, the upper rotor becomes a Left-Handed Rotor (LHR) and rotates clockwise. For a better comprehension of the coaxial setup, refer to Figure 3.3. Lastly, the electric motors used for rotating the blades are the Leopard LC5065 motors coupled to YGE 205HVT speed controllers and SM300-Series 3300 W DC power supplies. This configuration is capable of generating up to 13'000 RPM.

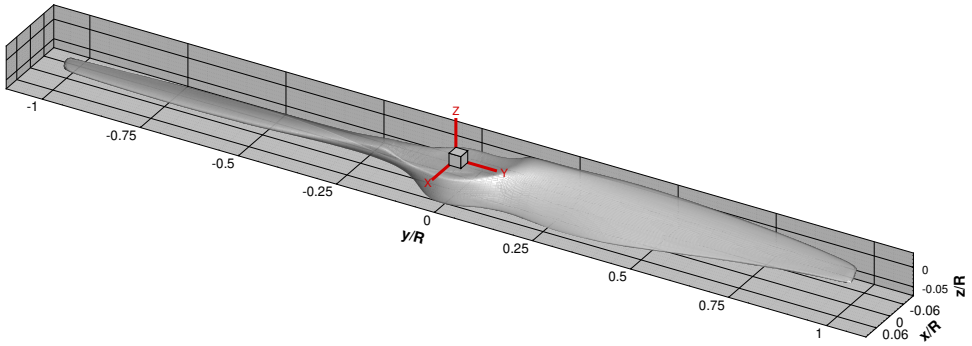

Figure 3.2: Isolated ISO view

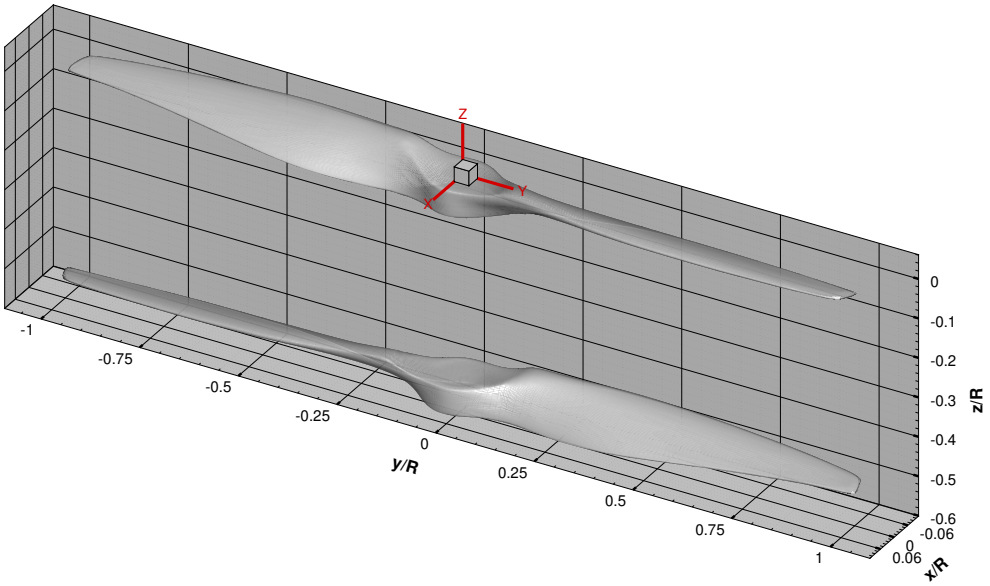

Figure 3.3: Coaxial ISO view

3.2. Set Up

As previously stated, there are two main configurations: the Isolated and Coaxial cases. For both configurations, the top boundary of the farfield is at a distance of $8R$ from the centre of origin, i.e., the rotor. Similarly, when putting the second blade for the coaxial configuration, this one is placed at $\Delta z = -0.5R$ from the upper one. Remember that the upper blade is the LHR and the lower, the RHR.
Two different conditions are being tested, but always keeping the hovering flight conditions, i.e., no free-stream velocity. The first one, the rotating speed is set at 8'000 RPM, which implies a tip Mach number of $M_{tip} = 0.40554$. Then, an increase in angular velocity is studied by setting the new angular velocity to 12'000 RPM, making $M_{tip} = 0.60830$.
The flow conditions are standardized to the International Standard Atmosphere (ISA) model at mean sea level.

3.3. Grid Generation

The meshing tool used to create the different grids and suitable for the ROSITA CFD solver is the commercial ANSYS ICEM CFD software. It is a pre-processing tool specifically designed for mesh generation in CFD, where its main key features are the already mentioned surface and volume meshing tool with the ability to create multi-block structures, unstructured or hybrid meshes; but it can also import and clean CAD geometries, check the grid's quality and generate boundary layer meshes.
As mentioned previously, interest lies in using multi-block structured grids (composed only of hexahedrons) to be able to use the Chimera method. However, creating structured meshes may lead to non-smooth properties of the cells' domain, and even the possibility of having negative volume elements. To avoid bad meshing, a quality check can be done in the different domains. A common type of quality check is the so-called *Determinant 2x2x2*: its value comes from the ratio of each cell of the smallest determinant of the Jacobian matrix divided by the largest determinant of the Jacobian matrix. The Jacobian matrix represents the local stretching and deformation of the mesh elements. The meaning of the Determinant 2x2x2 goes as follows: A value of 1 indicates a perfectly regular mesh; instead, a value of 0 suggests an element that is degenerated in one or more edges; negative values mean that the element is inverted. Hence, for a good-quality mesh, it is suggested to have at least a minimum value of 0.4-0.5, if it falls below a potential issue in the accuracy and reliability of the CDF simulation may occur. Once the respective meshes are created, their quality has been checked, and boundary conditions have been applied, the mesh can be exported in a CGNS format, which is accepted by ROSITA.

For the purpose of this research, three different grids have been created. The outer one as the farfield, a finer intermediate one to capture the effects of the wake, and lastly, a mesh surrounding the blade with the proper boundary layer refinement.

As mentioned in Section 2.1.1, there are two types of boundary conditions: *Farfield B.C.* or *Froude B.C.*. It is suggested that when working with hovering flight, the last condition is used to not have recirculation of the flow inside the domain. However, this condition only works for steady simulations and without relative motion between the grids. Since the coaxial configuration is being studied, an unsteady simulation must be performed, so, no Froude B.C. is valid. To avoid the recirculation of the flow, a very large farfield domain has been set. Thus, a cylindrical farfield with $r = 12R$ and $L = 24R$ is the outer grid (Figure 3.4a); being R the radius of the rotor blade ($R = 0.165$ m). Notice that to simplify the tagging process, a refinement of the grid near the rotor locations is needed, in this way, the elements of the two grids in the overlap region have similar dimensions.

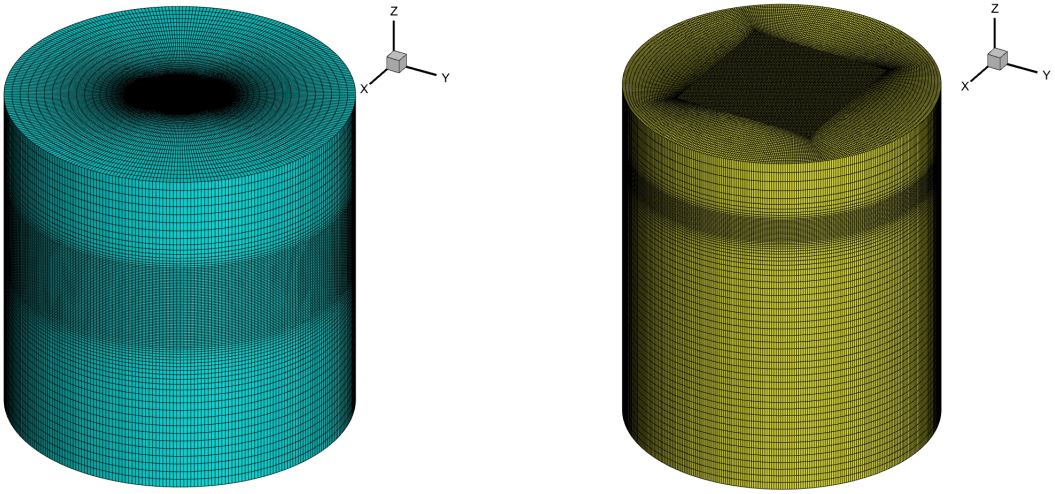

(a) Farfield mesh (b) Middle mesh

Figure 3.4: Background meshes

The middle grid, Figure 3.4b, intends to capture the effects of the rotor wake by refining the cells below the coaxial rotors, it also works as a transitional grid between the rotating blade meshes and the background grid. Its dimensions are $r = 2.6R$ and $L = 6R$. Figure 3.5 shows where the middle grid is located with respect to the farfield mesh.

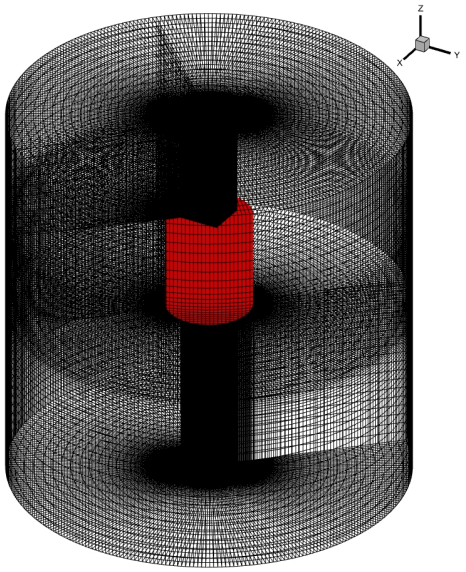

Figure 3.5: Placement of the middle mesh w.r.t. the farfield mesh

Lastly, for the blade grid, a boundary layer refinement has been established to capture the effects of this phenomenon (Figure 3.6), always keeping in mind that the minimum element dimension at the wall guarantees $y^+ \approx 1$. Around the rotor blade surface, a kind of O-grid has been created with a progressive increase in the size of the elements while moving away from the solid boundary. A cylindrical geometry was first thought for the farfield boundary, but elements experienced excessive deformation; that is why a rectangular prism was finally chosen. Figures 3.6 & 3.7 show the blade mesh and its different views.

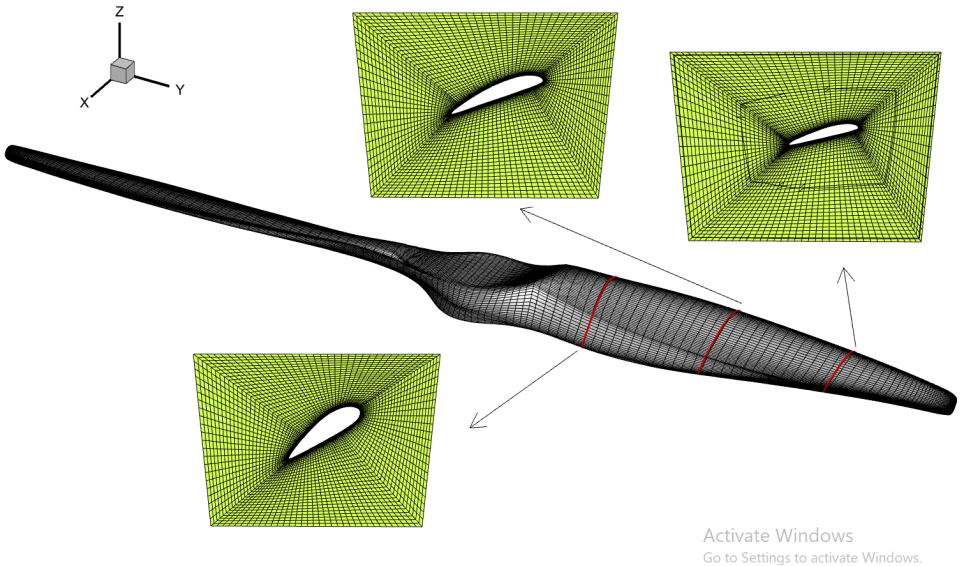

Figure 3.6: Boundary layer refinement visualization

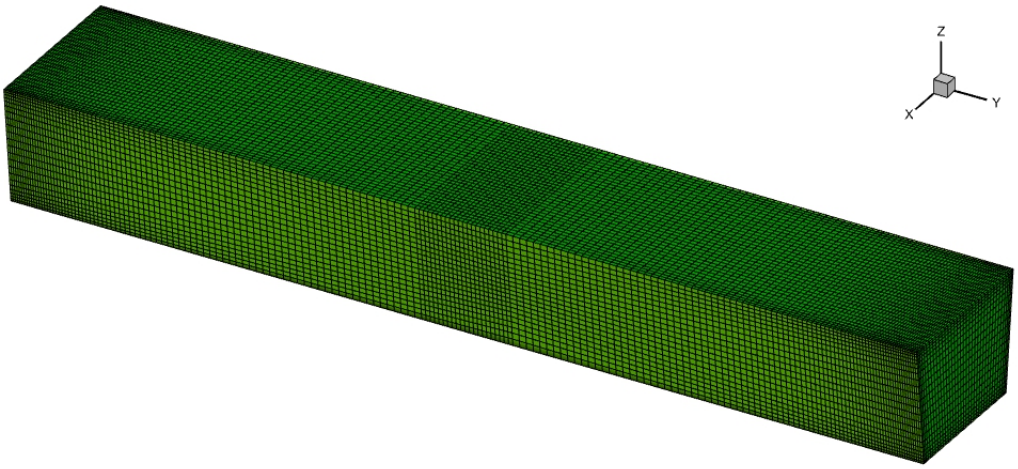

(a) ISO view

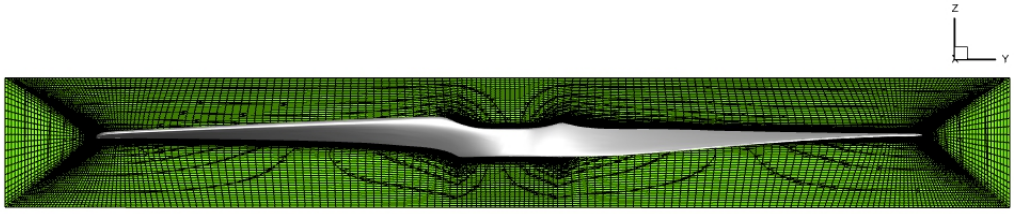

(b) OYZ plane

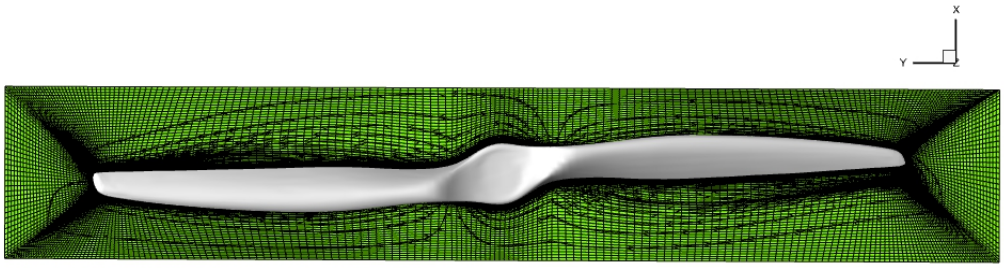

(c) OXY plane

Figure 3.7: Blade grid views

The blade geometry showed until now has a counter-clockwise motion, hence, is a right-handed rotor. When working with coaxial configuration, the upper blade spins clockwise, so the geometry is also different, but this is not a big issue, as a mirrored geometry and mesh have been created in ICEM. In short, 3 different types of grids are used to run the simulation. For the isolated case (just the right-handed rotor), only one blade is used (Figure 3.8a), however, for the coaxial configuration an upper LHR and lower RHR are used, with a distance of $\Delta z = -0.5R$ (Figure 3.8b).

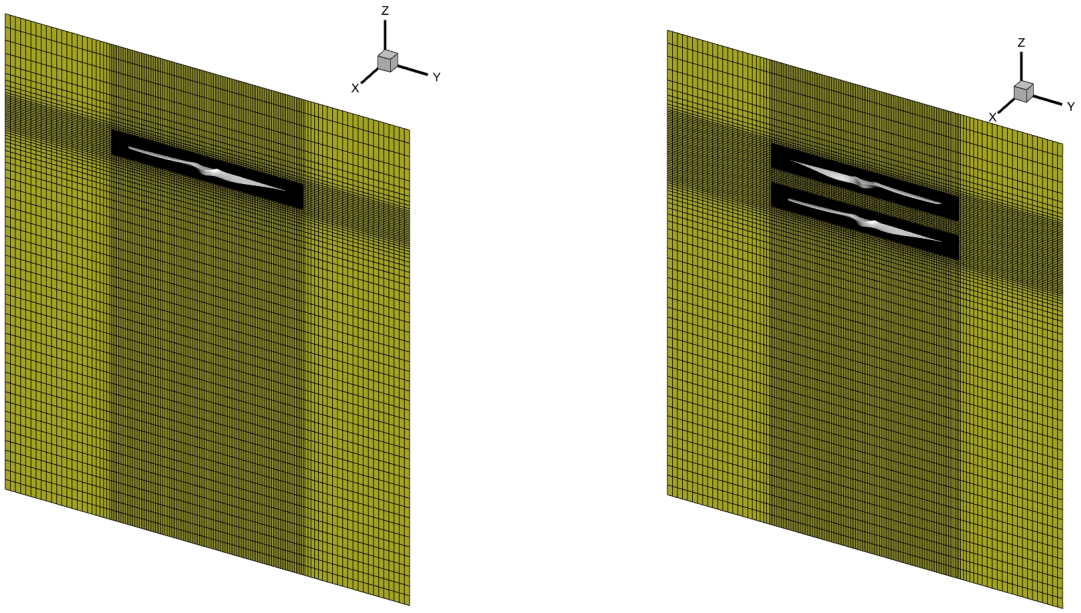

(a) Isolated configuration mesh (b) Coaxial configuration mesh

Figure 3.8: OZY planes of middle and blade meshes

For ROSITA to proceed with the tagging process as outlined in Section 2.1.2, it needs a prioritized grid specification. Given the primary focus near the blade, the hierarchy of grid importance is: first the blade grids, then the intermediate background, and last, the farfield mesh.
Another consideration is the scale factor within the grid file. It should be configured to normalize the reference length, specifically the rotor radius, to a value of 1. Lastly, for the boundary conditions, a no-slip condition has been chosen for the surface of the rotor blade; and as mentioned previously, the far-field condition has been set for the farfield grid.

3.4. Independence Analysis

Once the different grids have been described, it is time to talk about the number of elements of each grid and how should their refinements be. To ensure that the results obtained are not dependent on the different meshes used for the simulation, it is important to perform a mesh independence test. Notice that no change to the grids' dimensions have been made, only the total number of cells and their refinement have been modified.
A series of decisions have been made in order to follow a reasonable approach and make this analysis easy to conceive. It has been decided to fix the number of elements and refinements of the farfield grid and only vary the parameters of the mid and rotor blade

grids. Then, only two different blade meshes have been created, one being the finer one and the other, the coarser. Lastly, for the middle one, a fine, a medium, and coarse grids are built. Tables 3.1, 3.2 & 3.3 show the number of elements for each version.

Blade mesh	
	Nº of elements
Fine	1'923'720
Coarse	1'476'000

Table 3.1: Number of elements for the blade meshes

Mid mesh	
	Nº of elements
Fine	2'877'302
Medium	1'628'776
Coarse	989'300

Table 3.2: Number of elements for the mid meshes

Farfield mesh
Nº of elements
1'962'688

Table 3.3: Number of elements for the farfield mesh

To know which configuration has the least influence on the results, six different steady simulations for the Isolated case at 8'000 RPM have been done. Performing a steady simulation is possible since only one blade is used. This setting makes results converge faster, as there is no relative motion between the grids, and the tagging process is only done at the beginning, reducing computational costs. A mesh independence test has not been performed for the coaxial configuration, as it requires too much computational time. Hence, a comparison of the simulated time-averaged rotor thrust and torque for the last 5'000 iterations and its errors are presented in Tables 3.4 and 3.5. The error has been computed using the following formula (Eq. 3.1) taking the experimental value from DLR as a reference ($T = 24.677$ N and $M_z = -0.474$ Nm). Where i is for the current mesh, ref is for the experimental data, and X can be for T or M_z.

$$err^i_{\%} = \left| \frac{X^{ref} - X^i}{X^{ref}} \right| \text{ x } 100 \tag{3.1}$$

Fine blade mesh						
Mid mesh	Nº of cells	CPU time (h)	Thrust (N)		Mz (Nm)	
			Value	Err.(%)	Value	Err.(%)
Fine	6'484'888	39	21.182	14.16	-0.451	4.85
Medium	5'418'138	37	21.147	14.30	-0.450	5.06
Coarse	4'207'334	25	20.647	16.36	-0.438	7.59

Table 3.4: Relative errors for the finer blade mesh

Coarse blade mesh						
Mid mesh	Nº of cells	CPU time (h)	Thrust (N)		Mz (Nm)	
			Value	Err.(%)	Value	Err.(%)
Fine	6'040'140	35	20.842	15.54	-0.462	2.53
Medium	4'809'908	30	20.830	15.59	-0.461	2.74
Coarse	3'762'586	23	20.576	16.62	-0.463	2.32

Table 3.5: Relative errors for the coarse blade mesh

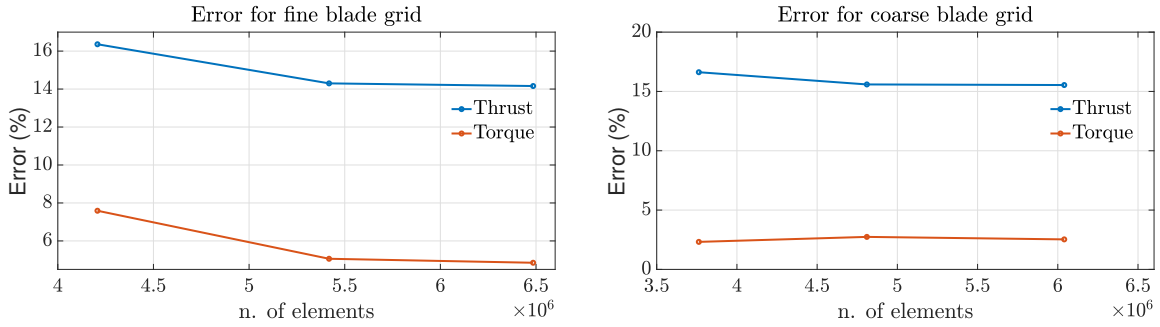

(a) Fine blade mesh relative errors

(b) Coarse blade mesh relative errors

Figure 3.9: Grid Influence errors plot

Looking at the above tables and plots it can be clearly seen that for the coarser blade gird, despite having a small error for the torque, the thrust error is the biggest of them all, hence, all the grids in Table 3.5 and the last row in Table 3.9a have been dismissed. Those values closer (with a small error) to the reference data are the ones when using the fine blade mesh. The last two remaining belong to the medium and fine middle background grids, while using the fine blade one. Having a look at the error, both values are similar, so no decisions can be made by just looking at this parameter; but, when looking at the CPU time, it can be seen that for the fine case, the computational cost is much higher, and more time is needed with respect to the medium one to obtain a similar

result. Hence, choosing the medium middle mesh with the finer blade grid appears to be the most optimal choice, as it has a good compromise between the fidelity of the results and the total computational cost.
Notice that when adding the second blade for the coaxial configuration, the number of cells has been kept constant, but some modifications on the refinement around the rotor blades have been done in order to capture better the effect of the rotor-rotor interaction. Hence, the final grid configurations for both Isolated and Coaxial configurations are shown in Figure 3.10, with a total number of elements of 7'694'571 for the coaxial configuration, and 5'418'138 for the isolated case. To see some data obtained from the final mesh configuration after doing a steady simulation, refer to Appendix A.1, where the residuals are plotted to check if the simulation has come to convergence (Figure A.1).

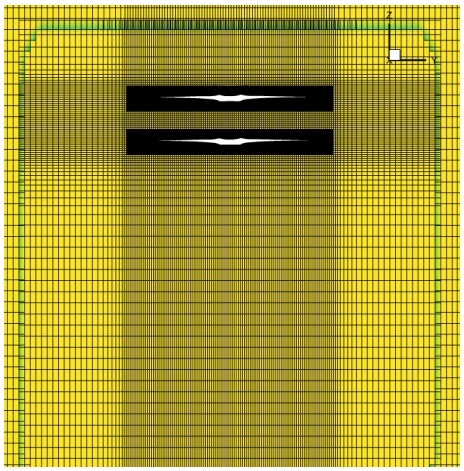

(a) OZY plane slice

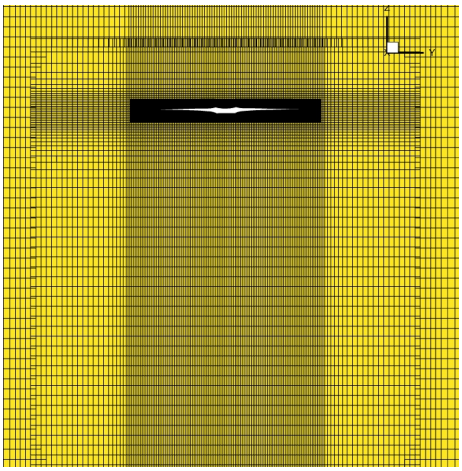

(b) OYZ plane slice

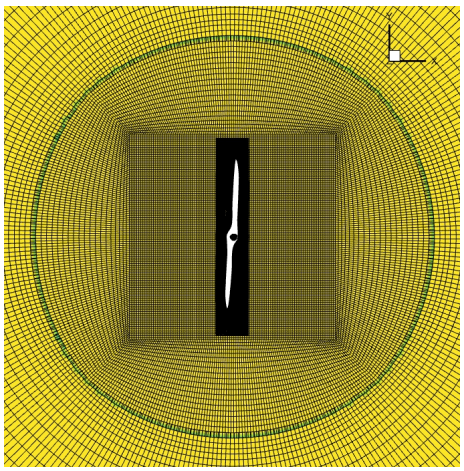

(c) OXY plane slice

Figure 3.10: Isolated and Coaxial final meshes

4 | Results & Data Comparison

In this chapter, the numerical simulation results are presented both for the isolated and coaxial configurations, along with a comparison against data obtained in [24]. The results for the isolated case are discussed, both steady (Section 4.1.1) and unsteady (Section 4.1.2), and compared with data in [24]. The same goes for the coaxial case, discussed in Section 4.2. Notice that not all the figures and tables are presented in the main sections, in Appendix A are included more figures to complement the main results.

Regarding the angular speeds for a hovering flight, the ones used are 8'000 RPM and 12'000 RPM. Some parameters have been kept the same for all the different simulations: the CFL for the mean flow equations has been set to a maximum of 2, while 0.4 for the S-A equation; and to speed up the process, the parallelization setup described in Section 2.1.2 it has been used with a total of 56 processors.

For the computation of the different loads, as described in Section 2.1.1, ROSITA prints non-dimensional values ($F_{nz(i)}$, $F_{tz(i)}$, $M_{nz(i)}$, $M_{tz(i)}$, $P_{(i)}$); hence, the final thrust, torque and pressure coefficients can be computed by applying the following equations:

$$C_{T(i)} = \frac{F_{nz(i)} + F_{tz(i)}}{M_{tip}^2 \pi} \quad \rightarrow \quad T_{(i)} = C_{T(i)} \rho V_{tip}^2 \pi R^2 \tag{4.1}$$

$$C_{Q(i)} = \frac{\omega \left(M_{nz(i)} + M_{tz(i)} \right)}{M_{tip}^3 \pi} \quad \rightarrow \quad M_{z(i)} = C_{Q(i)} \rho V_{tip}^2 \pi R^3 \tag{4.2}$$

$$C_{P(i)} = \frac{P_{(i)-\frac{1}{\gamma}}}{\frac{1}{2} M_{tip}^2} \tag{4.3}$$

Where the sub-index i is for every P-time. Thus, the final value is taken from the average of the last 5'000 iterations for the steady case, and the last 2 revolutions for the unsteady one, where the simulations have reached stability.

4.1. Isolated Rotor

4.1.1. Steady Case

To begin with the rotor aerodynamics study, the isolated steady configuration is the first to be computed, as it is the least complex and time-demanding of all the different cases. The final configuration chosen from the Independence Analysis in Section 3.4, has been used to compute the 8'000 rpm and 12'000 cases. To prove that the simulations come to convergence, some checks have been done during the computation. One check is the residual behaviour throughout the iterations (Figure 4.1), along with the thrust and torque coefficients behaviour, all plots shown below are for the 12'000 rpm case. Refer to Appendix A.1 to check the convergence of the 8'000 rpm case.

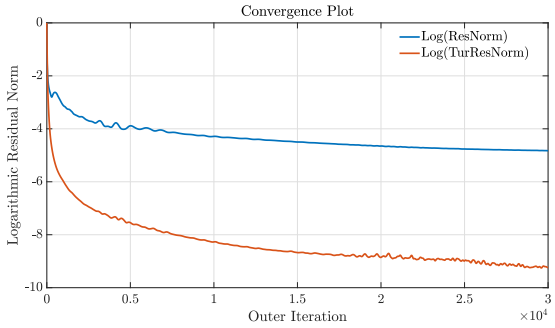

Figure 4.1: Residual values for steady isolated-12'000 rpm case

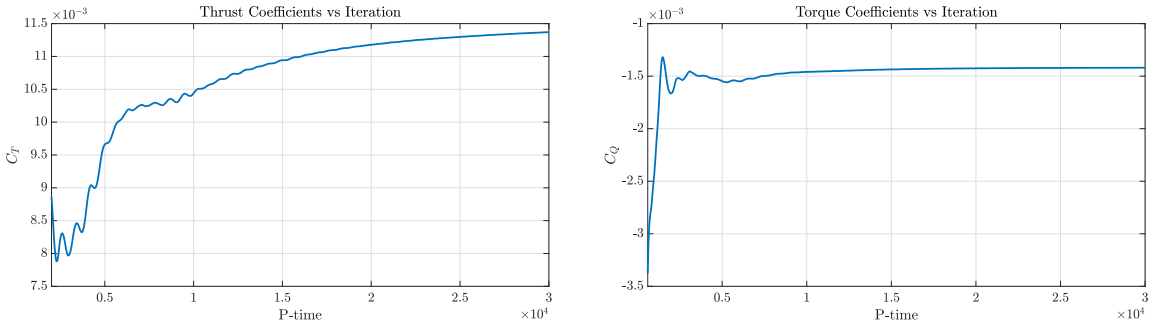

(a) Thrust coeff. convergence plot (b) Torque coeff. convergence plot

Figure 4.2: Numerical results vs revolutions for steady isolated 12'000 rpm case

After 30'000 iterations, the simulation arrives at a stable state, because the residuals tend to have smaller values throughout the iterations, and the load coefficients tend to a constant value (Figures 4.1 and 4.2). The computation has taken 37 hours to converge, hence, the CPU time for each iteration is: $\frac{37h}{30000iter} = 4.44$ sec/iter. Another verification to prove that the results are valid is by checking the value of y^+ at the last time step. Its

value given by the surface solution should be equal to or less than $y^+ \approx 1$. It is confirmed in Figure 4.3 that the values are not bigger than 1, for the 12'000 rpm case.

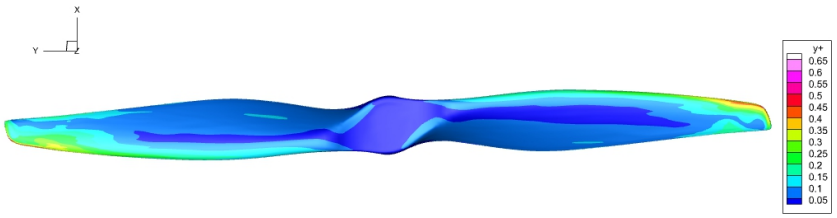

Figure 4.3: y^+ contour on the surface rotor

To know if the simulations are in good agreement with data from [24]; Table 4.1 shows the average value of thrust and torque for the last 5'000 iterations, and the experimental values obtained from the DLR AWB group.

	rpm	DLR Test	Steady Isolated
T (N)	**8000**	24.677	21.147
	12000	55.250	49.352
Mz (Nm)	**8000**	-0.474	-0.450
	12000	-1.127	-1.052

Table 4.1: Average values of the last 5'000 iter.

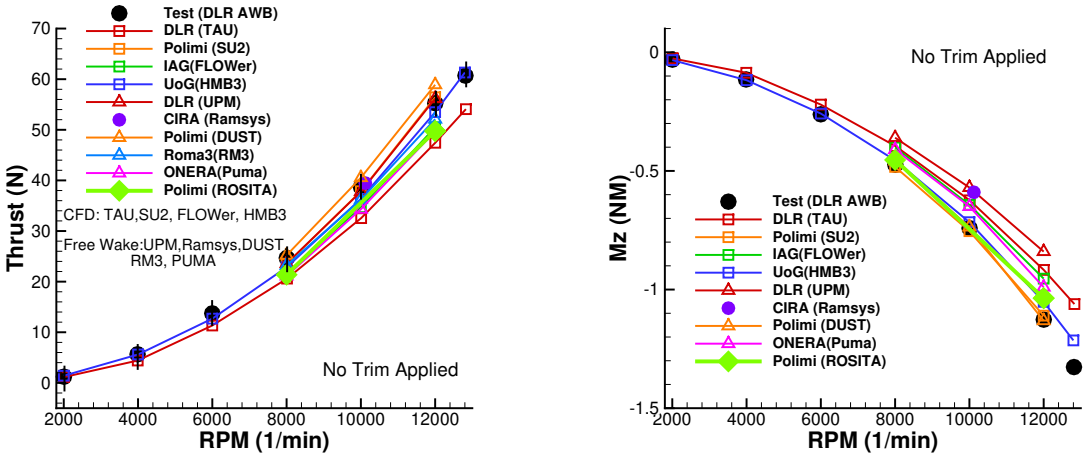

(a) Thrust vs Revolutions

(b) Torque vs Revolutions

Figure 4.4: Time averaged thrust and torque from [24] along with ROSITA's results

Figure 4.4, also shows the data obtained in [24] from all the different partners along with the ROSITA ones (green line). Evaluating those values, some conclusions can be made: good results have been obtained with the proposed ROSITA steady code, as they adjust to all computational and experimental data from Figure 4.4; the differences between the results of the tests are due to the precision of the different solvers, seeing a higher level of accuracy for the CFD codes. This last statement is due to the fact that CFD codes are able to capture flow separation, whereas mid-fidelity ones cannot. Also, a good grid resolution is crucial in CFD-related approaches to minimize computational errors.

Once the ROSITA's simulations have proven to be reliable for the last 5'000 iterations for the steady case, the flow field can be analysed. The 12'000 rpm case has been chosen, as the behaviour of the flowfield for the 8'000 rpm case is similar, hence, there is no preference of choice. Data from the following plots is extracted from the last time step of the steady simulation.

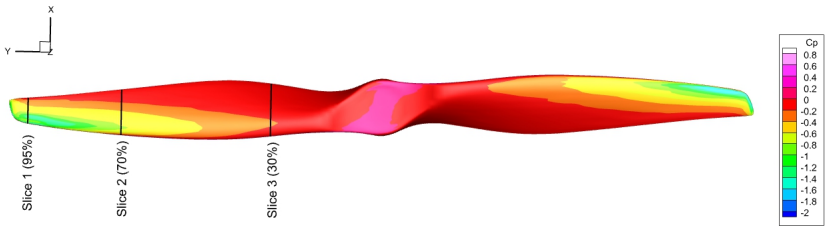

Figure 4.5: Pressure coefficient contour for steady 12'000 rpm

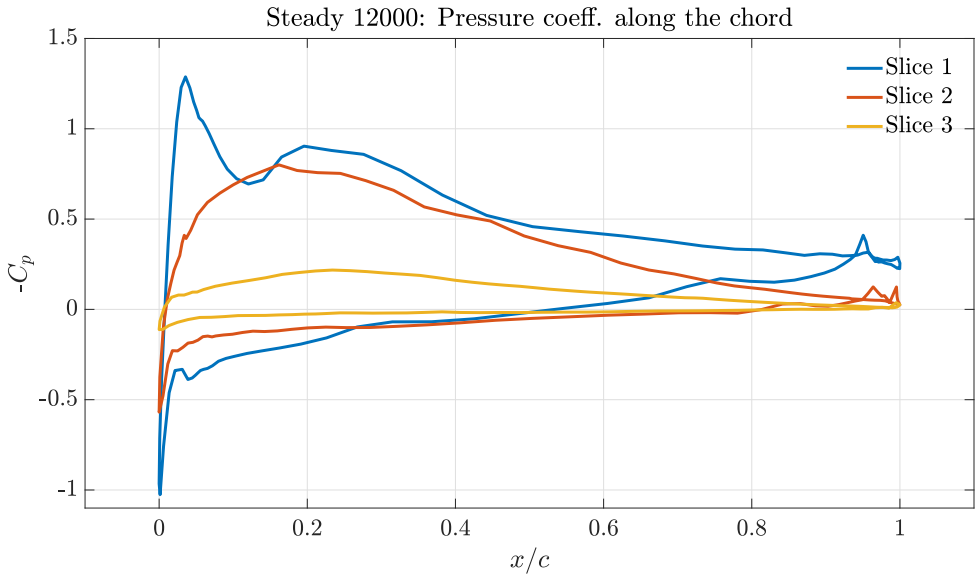

Figure 4.6: Pressure coeff. vs normalized chord for steady 12'000 rpm

As mentioned in the previous statement, a flow separation phenomenon occurs across the rotor that is captured by the code, and to verify it, the pressure coefficient on the surface of the blade has been plotted. Figures 4.5 & 4.6 show the C_P in three different locations: one near the tip at a 95% of the blade span (Slice 1), one in the middle at a 70% (Slice 2), and lastly, the one near the root at a 30% (Slice 3). Looking at the 3rd slice, it can be seen that loads in this region are not significant as there is little difference in pressure between the upper and lower surfaces. For the middle position, a more standard behaviour is observed, having a progressive decrease in pressure at the leading edge and a pressure recovery while approaching the trailing edge. For the last slice at the tip of the rotor blade, due to high velocities, a strong suction peak that involves an intense pressure gradient occurs, followed by a second, less intense, suction peak. Figure 4.7 represents these suctions peaks as the blue regions on the upper surface.

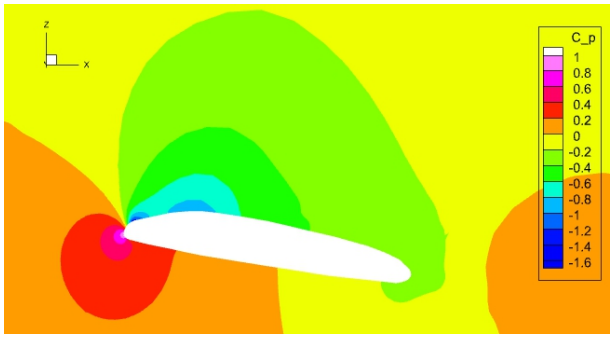

Figure 4.7: Pressure coeff. contour at 95% of the blade span

This last behaviour is mainly caused by the non-smoothness of the blade surface, generating harsh edges. Hence, a check on the original geometry has been done. Figure 4.8a shows the blade profiles of the three different slices, revealing that the tip's profile is the less aerodynamic one, resembling more like a bluff body (Figure 4.8b), hence, causing bad aerodynamics.

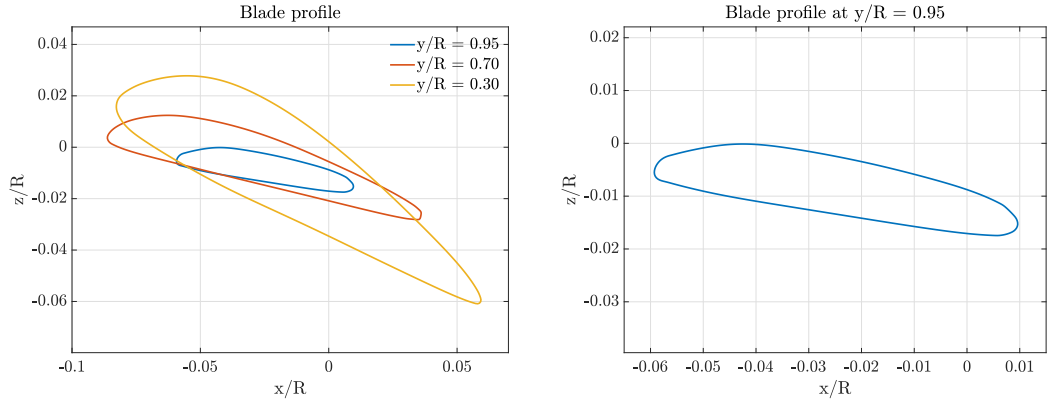

(a) Studied blade profiles

(b) Slice 3 close-up

Figure 4.8: Geometry profile of the different slices

Figure 4.9 shows the acceleration of the fluid when passing through the first sharp edge (first red circle) causing the strong peak suction, then a slowing down (2D compression), followed by a second acceleration due to the second sharp edge causing, afterwards, a boundary layer separation.

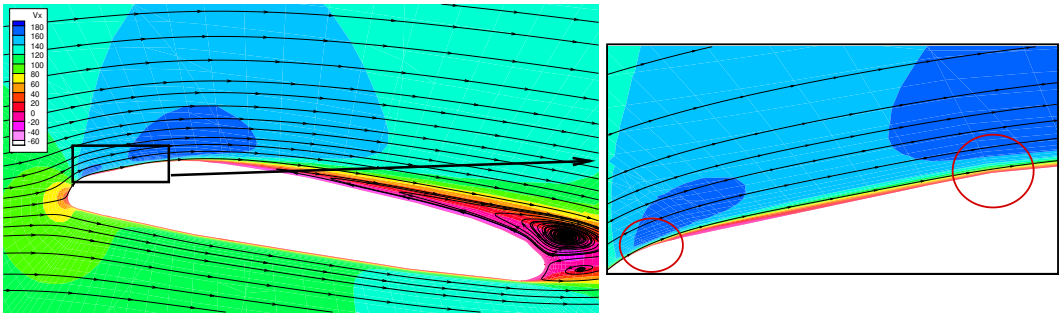

Figure 4.9: V_x contour at 95% of the blade span along with pseudo-streamtraces

Another zoom into the V_x contour plot is shown in Figure 4.10, which shows that in that region, the boundary layer separates from the wall, due to the non-smoothness of the surface, creating a recirculating region due to the adverse pressure gradient.

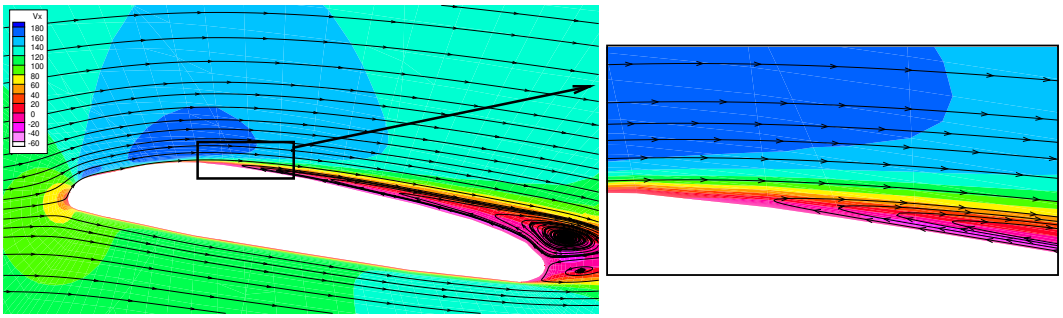

Figure 4.10: Boundary layer visualization, V_x contour at $y/R = 95\%$

Now that it has been proven that the code has captured the flow separation at the rotor blade surface; it is time to examine the wake region, as the main objective of this work is the rotor-rotor interaction. Figure 4.11 shows a colour map of the vertical velocity along with pseudo-stream traces, offering a comprehensive view of the flow field characteristics. Remember that for the steady case, the *Froude B.C.* can be applied in order to avoid the recirculation of the flow in the downstream wake region, which might extend very close to the rotor disk; and as checked in Figure 4.11 there is no recirculation near the rotor that can modify the rotor's performance. Another feature of the rotor wake has been captured: the mean velocity presents the characteristic contraction of the wake immediately downstream of the rotor disk. Lastly, a little attached vortex at the centre of the rotor is present.

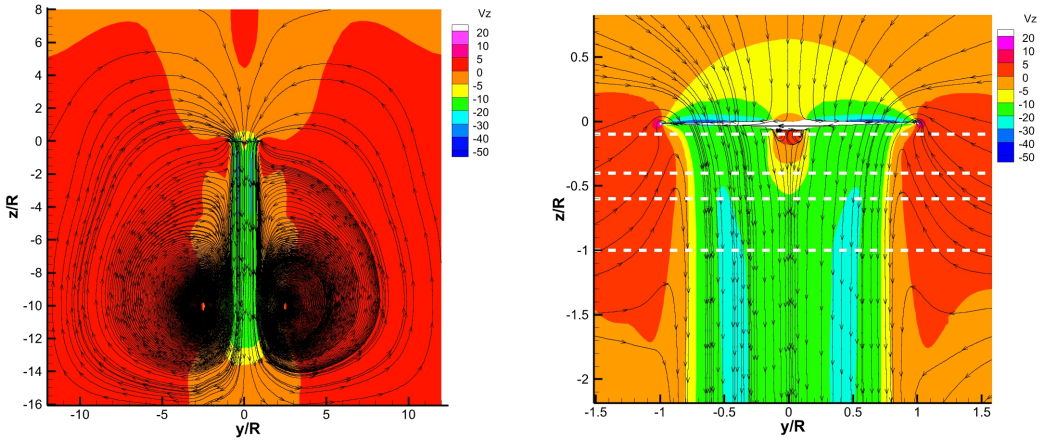

(a) Farfield pseudo-streamlines (b) Rotor close-up

Figure 4.11: OYZ plane: V_z contour along with pseudo-streamtraces

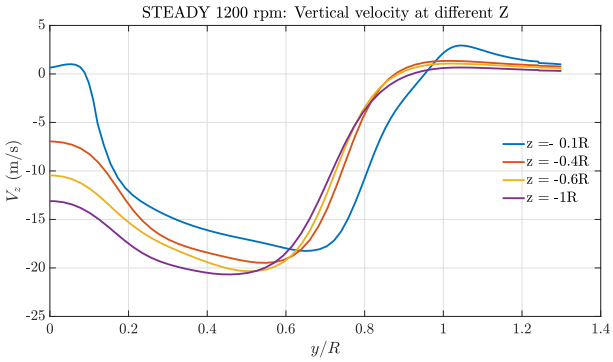

Figure 4.12: V_z trend along radial distance for different z for the steady 12'000 rpm case

Figure 4.12 shows the wake contraction by representing the vertical velocity in different z-planes (white dashed lines in Figure 4.19) along half of the rotor blade diameter (y/R>0). The velocity slope and flow acceleration in the shear layer region seems to be well captured, as the radial extension of the shear layer gets reduced, and a more gradual velocity slope appears when moving away from the rotor. The vortex root is also captured by the slow velocity of the fluid at the rotor axis.

Now that the focus is put on the wake region, identifying its characteristic vortices is a good practice. They are also called coherent structures. The visualization of these structures can provide valuable information about the flowfield and how it behaves, but identifying them can be sometimes tricky. There are many different criteria to determine a vortex [12], among them:

- *Minimum local pressure*: In a vortex, the pressure typically shows a local minimum along the axis when the centrifugal force is counterbalanced by the pressure force.

However, a scale disparity exists between the vortex core and the corresponding low-pressure region, hence, using iso-pressure surface can be problematic. As an example, in Figure 4.7, a kind of vortex at the T.E. can be seen when C_P is plotted.

- *Vorticity magnitude*: It visualizes the CS through the vorticity component:

$$\| \omega \| = \sqrt{\omega_x^2 + \omega_y^2 + \omega_x^2} \tag{4.4}$$

However, sometimes it cannot distinguish between a shear layer (as the flow in the boundary layer) and a vortex.

- *Q-criterion* [3]: it is based on the analysis of the velocity field, more specifically, on the velocity gradient tensor:

$$\nabla V = \frac{\partial u_i}{\partial x_j} = \frac{1}{2}\left[\left(\frac{\partial u_i}{\partial x_j}\right) + \left(\frac{\partial u_j}{\partial x_i}\right)\right] + \frac{1}{2}\left[\left(\frac{\partial u_i}{\partial x_j}\right) - \left(\frac{\partial u_j}{\partial x_i}\right)\right] \tag{4.5}$$

That it can be decomposed into a symmetric part, S, as the rate of deformation or the *strain rate tensor*, and an anti-symmetric part, Ω, as the rotation rate or vorticity tensor:

$$S = \frac{1}{2}\left[\left(\frac{\partial u_i}{\partial x_j}\right) + \left(\frac{\partial u_j}{\partial x_i}\right)\right] \tag{4.6}$$

$$\Omega = \frac{1}{2}\left[\left(\frac{\partial u_i}{\partial x_j}\right) - \left(\frac{\partial u_j}{\partial x_i}\right)\right] \tag{4.7}$$

So, ∇V has 3 invariants:

  - D: captures the flow compressibility by its determinant

$$D = \frac{\partial u_i}{\partial x_i} \tag{4.8}$$

  - Q: Q-criterion that relates the rotational nature of the flow, with values grater than zero meaning a dominance of enstrophy over strain, while negative values imply the opposite.

$$Q = \frac{1}{2}\left(\frac{\partial u_i}{\partial x_i}\frac{\partial u_i}{\partial x_i} - \frac{\partial u_i}{\partial x_j}\frac{\partial u_j}{\partial x_i}\right) = \frac{1}{2}\left(\| \Omega \|^2 - \| S \|^2\right) \tag{4.9}$$

    Where: $\| \Omega \| = \sqrt{tr\left(\Omega\Omega^T\right)}$ and $\| S \| = \sqrt{tr\left(SS^T\right)}$

  - R: The last invariant depends on strongly to Q. For $Q > 0$, $R < 0$ represents vortex stretching and $R > 0$ vortex compression. In the limit of large negative

values of Q however, R is dominated by the self-amplification. Lastly, positive and negative values of R mean sheet-like and tube-like structures respectively.

$$R = Det\,(\nabla V) \tag{4.10}$$

Hence, as Q represents the local balance between shear strain rate and vorticity magnitude, it can be seen that positive values of Q indicate areas in the flowfield where the vorticity dominates, and negative values of Q are indicative of strain rate or viscous stress-dominated areas. In conclusion, *Q-criterion* is a Galilean invariant used to visualize 3D vortical structures using iso-surfaces of Q values, but keeping in mind that the quality of visualization depends on the selected threshold level of Q value.

Now that the different types of vortex visualization have been explained, they can be applied in the current simulation.

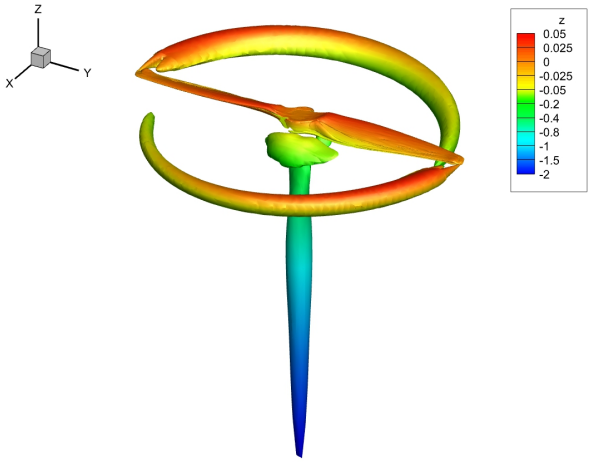

Figure 4.13: ISO-surfaces for the Q-Criterion (Q = 0.06), along with z contour

Figure 4.13 shows the different coherent structures when using the iso-surfaces for the Q-criterion (Q = 0.06). With this visualization, a vortical helicoidal structure can be observed, due to the tip vortices; a trailing edge vortex sheets; and also, a central vertical vortex due to the root part of the rotor blade, that extends downstream, where it has already been seen in the stream traces and vertical velocity plots. Lastly, as this rotor works in hovering conditions, the tip vortices do move a little downstream due to the induced downwash velocity, however, there exists some bade vortex interaction. All of these vortical structures and their movement downstream are of crucial importance when further studying the coaxial configuration, as the vortices from the upper rotor are going to interfere with the lower rotor changing its performance.

4.1.2. Unsteady Simulation

For the unsteady simulation, some parameters have been introduced or changed regarding the steady ones. The simulations have been initialized as a steady state, with 500 P-time steps. Then, 5 revolutions for the isolated case and 7 revolutions for the coaxial were required to achieve a periodical/stable state, with an incremental azimuthal angle of 1 degree and 50 pseudo-time steps for each azimuthal step. The tagging process has been only done once at the beginning, for only one revolution at each azimuthal angle, as it has a periodical behaviour in every complete revolution and the same tagging can be used.

Two simulations, 8'000 rpm and 12'000 rpm, have been also computed. To check if they have achieved stability, it is good practice to look at the residuals plot for the 8'000 rpm case, for example (Figure 4.14), where the darker vertical lines represent one complete revolution. For the last two revolutions, a periodical behaviour is observed. Another check that can be done is the load convergence as shown in the previous section, in this case, refer to Appendix A.2, where the residual convergence for the 12'000 rpm, and the loads' evolution for the 8'000 rpm and 12'000 cases are shown. To do 5 revolutions, for both simulations, it took a total time of 88 hours $\approx$ 3,6 days; hence, a CPU time for each iteration of 3.5 sec/iter.

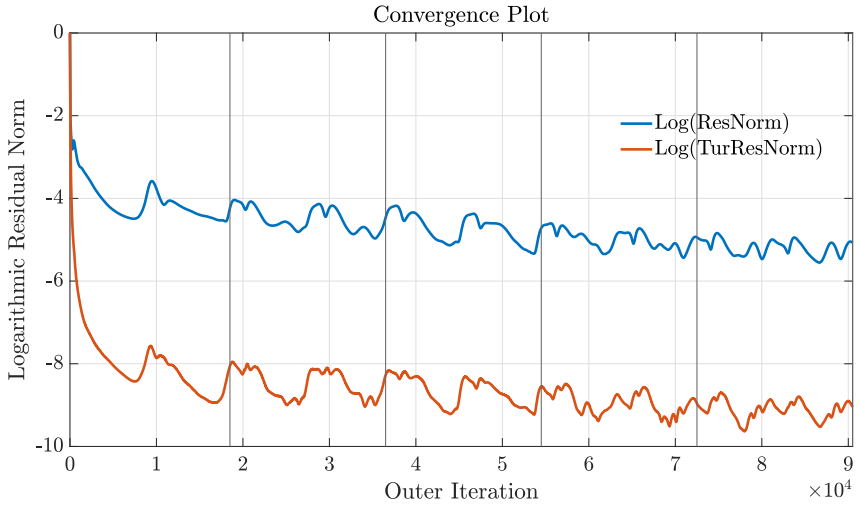

Figure 4.14: Residual for unsteady isolated-8'000 rpm case

As done in Section 4.1.1, to prove the validity of the results, the y^+ value has been checked at the last time step ($\Phi = 1800^{\circ}$) for both cases. It is again confirmed in Figure 4.15 that the values are not bigger than 1, both for the 8'000 rpm and 12'000 rpm cases.

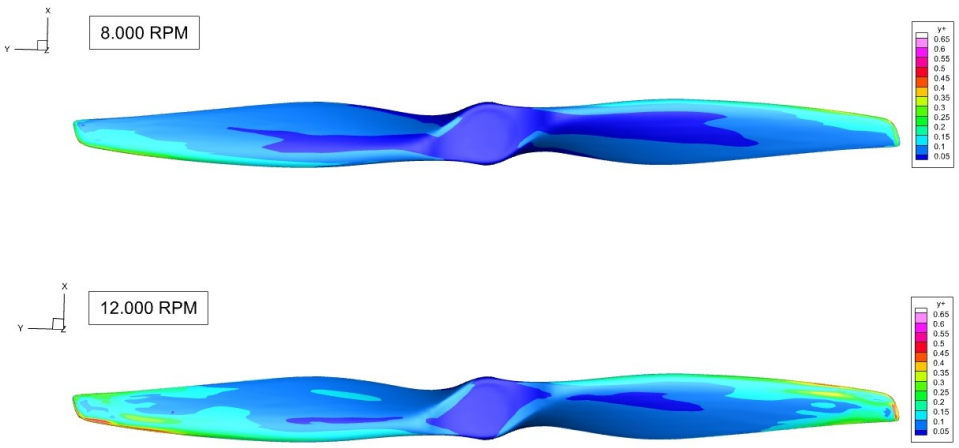

Figure 4.15: y^+ map on the surface rotor

To prove that the simulations are in good agreement with other results, all data collected so far has been put on Table 4.2:

	rpm	DLR Test	Steady Isolated	Unsteady Isolated
T (N)	**8000**	24.677	21.147	21.369
	12000	55.250	49.352	49.759
Mz (Nm)	**8000**	-0.474	-0.450	-0.453
	12000	-1.127	-1.052	-1.036

Table 4.2: Average values of the last 2 revolutions

If the isolated unsteady case results are being compared with the previous steady simulation, at 8'000 rpm and 12'000 rpm, it can be seen that they are in good agreement, as the average value of thrust and torque for the last 2 revolutions are similar to the steady case. Having a look at Figure 4.4 from the previous section, data from the experimental and computational cases in [24] are similar to the unsteady cases.

Once the reliability of the isolated unsteady simulations has been proven, both for 8'000 rpm and 1'2000 rpm, the flow field can be analysed and compared with the steady case. Hence, to be in accordance with the steady study, the 12'000 rpm case is being discussed. Data is extracted from the last time step, being the azimuthal angle $\Phi = 1800^{\text{o}}$, meaning that is the last position of the 5th revolution.

Similar to the preceding section, the pressure coefficient along the chord for different positions of the rotor blade span are being computed. Thus, some conclusions can be made by comparing these results with the steady ones.

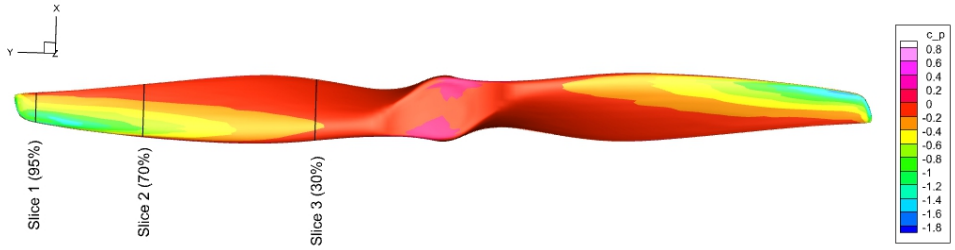

Figure 4.16: Pressure coefficient contur

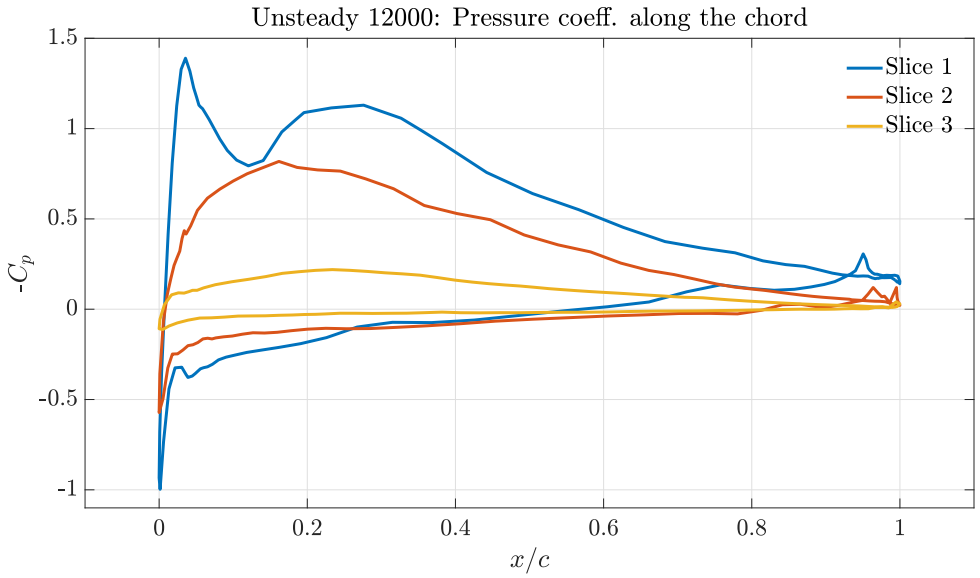

Figure 4.17: Pressure coeff. vs normalized chord

The plot in Figure 4.17 has the same shape as in the steady case, in other words, the pressure coefficient at the rotor surface behaves similarly for both setups. Since for the steady and unsteady cases, their blade grid rotates, the flow around their rotor surfaces has the same pattern. However, keep in mind that for the unsteady case, there is a relative motion between the blade grid and the intermediate one. Thus, when moving away from the rotor, for the unsteady case, there are different interpolated cells for each azimuthal angle, which causes the solution to differ from the steady one, where there is no relative motion between grids and the interpolated cells remain the same along the iterations.

Now, the pressure coefficient for the 8'000 rpm and 12'000 rpm unsteady cases are being compared in Figure 4.18 to see how the pressure behaves in different conditions.

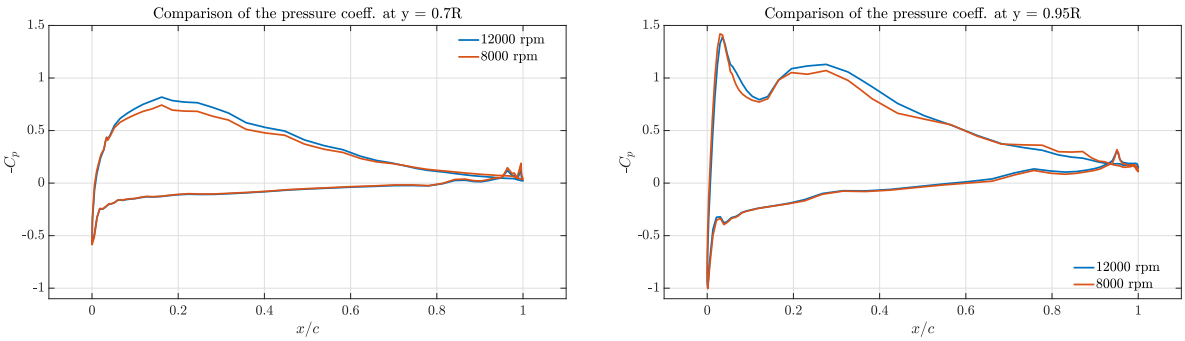

(a) C_p vs x/R at y = 0.7R (b) C_p vs x/R at y = 0.95R

Figure 4.18: Pressure coeff. comparison for 8'000 rpm and 12'000 rpm

For the 12'000 rpm case, as the speed is higher, the difference of pressure between the lower and upper is greater in comparison with the 8'000 rpm case, resulting in a higher thrust. This behaviour is captured in the above plots, as the total area of the blue line (12'000 rpm case) is bigger than the 8'000 rpm case. Moreover, a smoother behaviour of c_p along the upper and lower surfaces for the 12'000 rpm case can be seen.

The wake region is being again studied by plotting the colour map of the vertical velocity along with its pseudo-streamtraces.

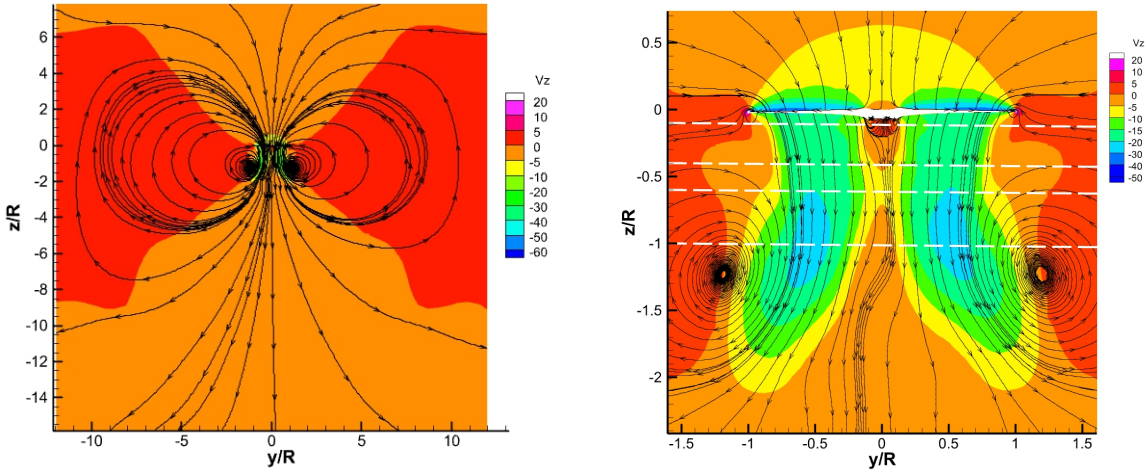

(a) Farfield pseudo-streamlines (b) Rotor close-up

Figure 4.19: OYZ plane: V_z contour component along with pseudo-streamtraces

For the unsteady case, the *Froude B.C.* at the far-field is not yet implemented, hence, it has been used the *Farfield B.C.*, making the flow to recirculate near the rotor disk as it can be seen in Figure 4.19a. Another aspect to take into account, when working with unsteady

simulations, is the presence of vortices near the rotor disk for the first revolutions, making the wake flow field region not have a steady behaviour. These vortices move downstream and dissipate as more revolutions are simulated. Having a look at Figure 4.19b, those vortices can be clearly seen near the rotor, hence, more revolutions need to be computed to obtain a stable wake region flow field. The wake contraction has been also captured by looking at the inward deflection of the pseudo streamtraces.

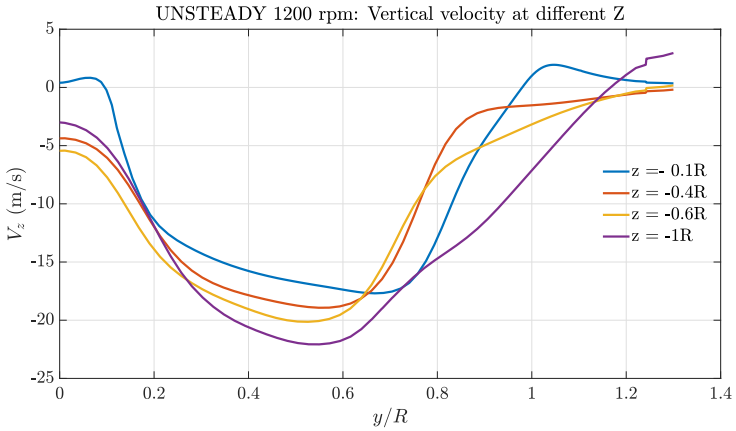

Figure 4.20: Vertical velocity trend along radial distance for different z

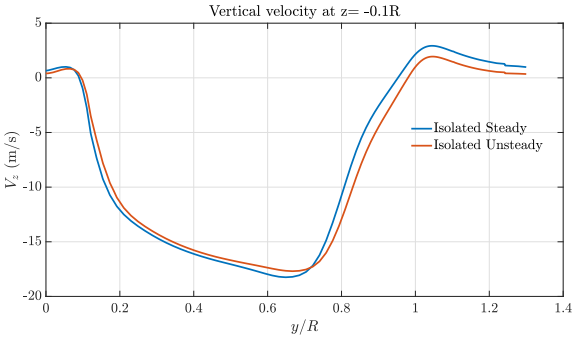

(a) Vertical velocity at z = -0.1R

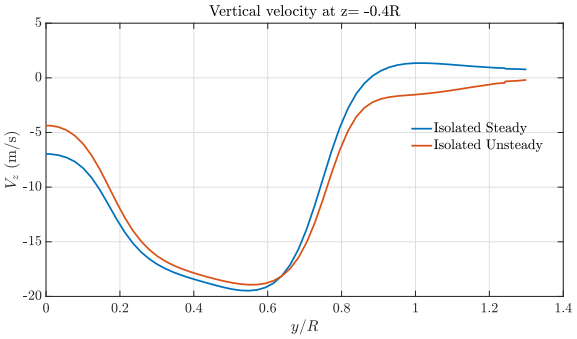

(b) Vertical velocity at z = -0.4R

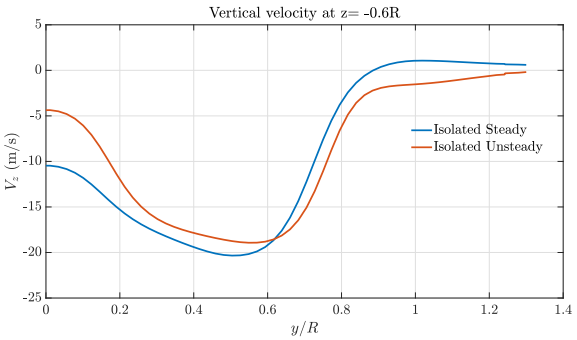

(c) Vertical velocity at z = -0.6R

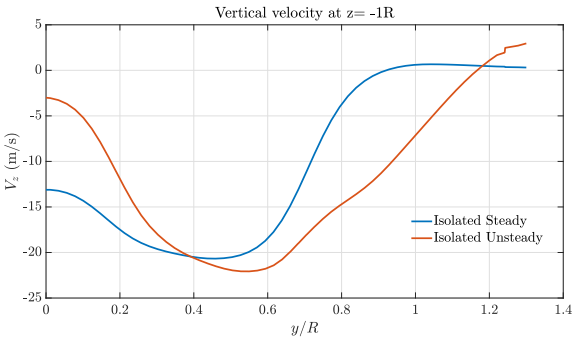

(d) Vertical velocity at z = -1R

Figure 4.21: Steady vs Unsteady comparison of vertical velocity at different z

Figure 4.20 shows the vertical velocity trend in different z for the unsteady 12'000 rpm case, along with a comparison with the steady case for each z (Figure 4.21). For the first two z-planes, the vertical velocity has the same behaviour as for the steady, but when moving downstream the dissipation of the wake region is stronger due to the presence of the fluid recirculation wake vortices. This trend gets intensified at $z = -1R$, Figure 4.21d, where for the steady case the wake shear layer is still well-defined, instead, for the unsteady case, the wake region is being dissipated by moving the fluid outwards and decelerating the fluid at the centre (y/R = 0). Hence, more revolutions are needed in order to obtain a similar shear layer wake region as the steady case. The little vortex attached in the centre of the rotor disk is also captured in the plot around $y \approx 0$.

Lastly, Figures 4.22 & 4.23 show the visualization of the coherent structures using the Q-criterion and Vortex Magnitude criterion respectively.

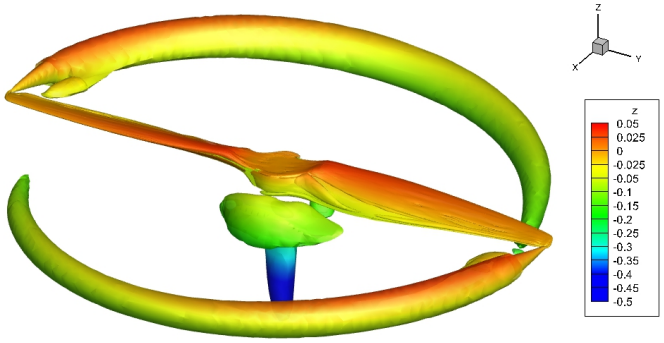

Figure 4.22: ISO-surfaces for the Q-Criterion (Q = 0.06), along with z contour

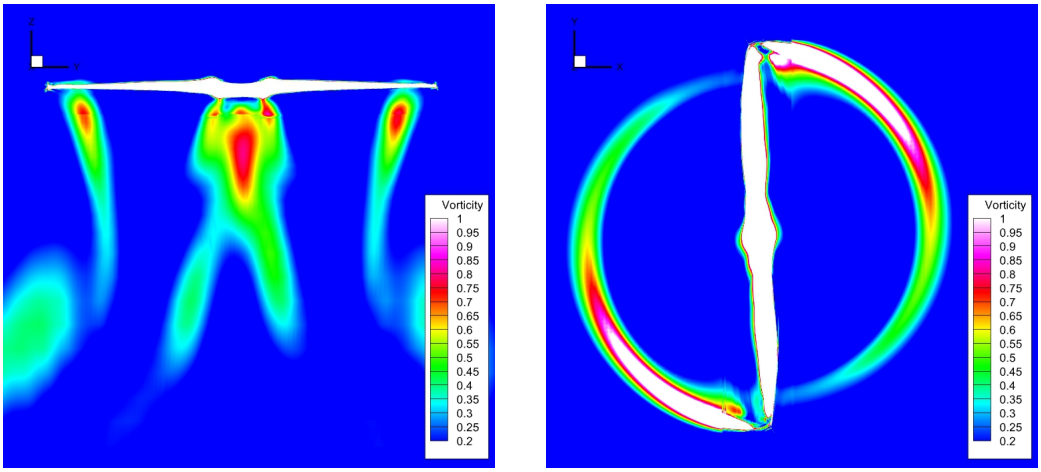

(a) OYZ plane (b) OXY plane

Figure 4.23: Vorticity magnitude visualization

Despite having similar shapes both steady and unsteady, a much shorter root vortex is captured when plotting the Q-criterion for the unsteady case, mainly due to the wake dissipation. The evolution and shedding of these vortical structures are shown in Figure 4.23a, at OYZ plane, when using the vorticity magnitude contour plot. It can be noticed the dissipation of the tip and root vortices, along with the wake, due to the recirculation effect. Also, some blade vortex interaction can be appreciated when looking at the OXY-plane of the rotor disk in Figure 4.23b. However, this way of visualizing the vortical structures is not entirely reliable as it cannot distinguish well between the tip, root, and trailing edge vortices and the wake shear layer.

4.2. Coaxial Rotors Configuration

Once the performance of the isolated rotor has been analysed, it is time to add a second rotor to evaluate the performance of the coaxial configuration. As mentioned in Section 3.1, the lower blade is placed at Δz= -0.5R, where the upper rotor spins clockwise, and the lower one counter-clockwise. A total of 7 revolutions has been computed for the 12'000 rpm case. The total computational time has been around 135 hours = 5.6 days. Thus, to obtain a periodical behaviour, as it can be seen in Figure 4.24, it has been needed a total of 90'500 iterations, meaning that the time for iteration is 5.37 sec/iter. Refer to Appendix A.3 to see the residual plot for 8'000 rpm.

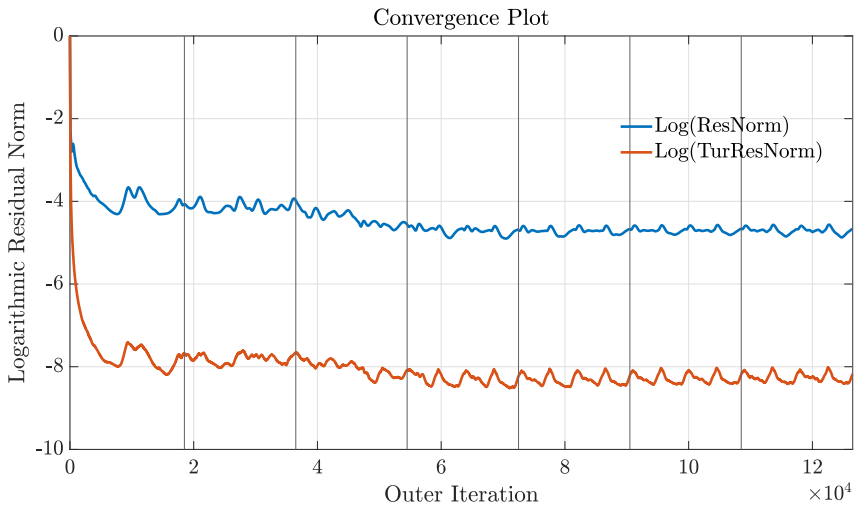

Figure 4.24: Residual for coaxial-12'000 rpm case

Thrust and torque have been computed by doing the values' average for the last 2 revolutions. The difference in performance for each rotor and condition (Table 4.3) have been calculated using Eq. 3.1 with the values obtained for each rotor in the coaxial config-

uration (T_{upper}, T_{lower}, $M_{z_{upper}}$, $M_{z_{lower}}$), w.r.t. the unsteady isolated case (T_{iso}, $M_{z_{iso}}$), obtaining the following data for both upper and lower rotors:

	rpm	Upper rotor	Lower rotor
Thrust difference (%)	**8000**	-2.3	-17.5
	12000	-3.2	-16.6
Torque difference (%)	**8000**	0.22	1.98
	12000	1.06	3.19

Table 4.3: Loads differences (%) for each rotor in the coaxial conf. w.r.t unsteady iso

	rpm	DLR Test	Steady Isolated	Unsteady Isolated	Coaxial	
					Upper rotor	Lower rotor
T (N)	**8000**	24.677	21.147	21.369	20.88	17.63
	12000	55.250	49.352	49.759	48.16	41.19
Mz (Nm)	**8000**	-0.474	-0.450	-0.453	-0.455	-0.563
	12000	-1.127	-1.052	-1.036	-1.047	-1.069

Table 4.4: Average values for all cases studied

Table 4.4, shows the average thrust and torque values for all different computed configurations, along with the DLR test results. At first glance, for the coaxial configuration, one can detect a loss of thrust on the lower rotor compared with the upper one for both conditions, 8'000 and 12'000 rpm. This behaviour primarily results from the impact of the downwash from the upper rotor, where the upper-induced velocity causes a reduction of the effective angles of attack of the lower rotor. Additionally, there is a slight reduction of the upper rotor thrust because of the mutual interaction with the lower rotor. Also, a small increase in torque magnitude for every condition has been captured, mainly due to the vortex interaction. All these behaviours will be better explained further in this section. But first, it is necessary to verify whether the simulation results are in accordance with the data from [24]. A comparison of the simulated and measured results obtained in [24] for the coaxial configuration, along with the values of the isolated rotor, are shown in Figure 4.25.

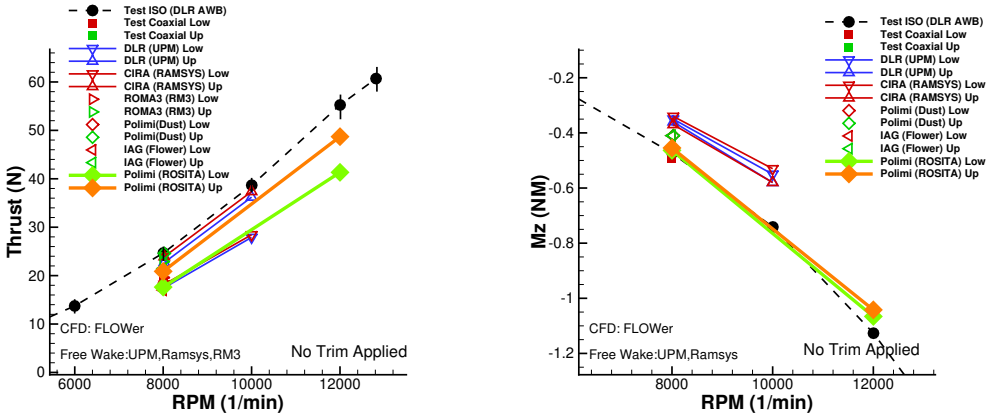

(a) Thrust vs Revolutions

(b) Torque vs Revolutions

Figure 4.25: Time averaged T and M_z from [24] for coaxial case with ROSITA's results

Good results have been obtained from the ROSITA code for the 8'000 rpm case, as it has well captured the loss of the lower rotor, and the obtained values are in accordance with the partners' results. No numerical computations were done for the 12'000 rpm case in [24], only experimental tests from DLR.

Now that the validation of the simulation has been done, it is time to analyse the data obtained. Again, the 12'000 rpm case is being discussed. All values from this section are taken from the last pseudo-time step of the last azimuthal angle, $\Phi = 2520^{o}$, which corresponds to an overlapping blade position. Figures 4.26 & 4.27 show the thrust and torque coefficients of the upper, lower, and isolated rotors versus the revolutions. An oscillating behaviour is perceived throughout a revolution, for the coaxial case. A characteristic of the coaxial rotors is the mutual aerodynamic interference between the upper and lower rotor, where, this behaviour is associated with the periodical passage of the blades over each other (4 times per revolution: 0^{o}, 90^{o}, 180^{o} and 270^{o}), resulting in a pulsation in the aerodynamic loads. These pulsations do not appear when having an isolated configuration (blue line).

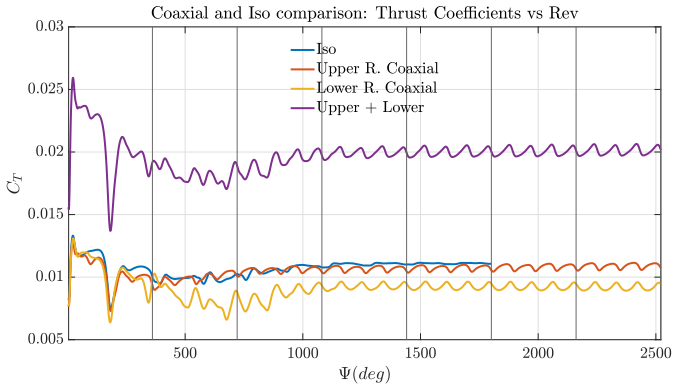

Figure 4.26: C_T comparison for isolated, upper, lower, and both rotors

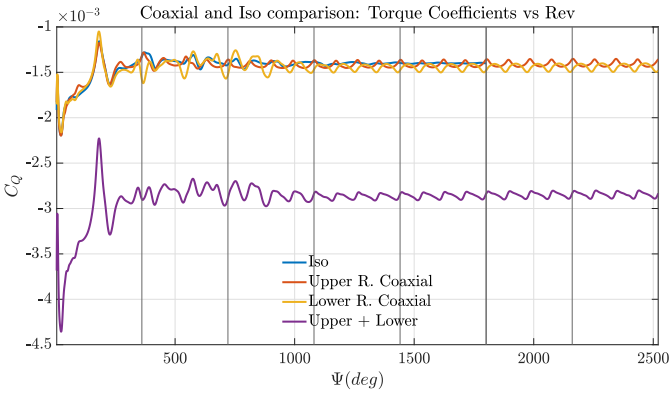

Figure 4.27: C_Q comparison for isolated, upper, lower, and both rotors

Notice that for the isolated unsteady case, only 5 revolutions have been computed.

To better understand the rotor-rotor interference of two contra-rotating rotors, and how the dynamics of each rotor modify the flowfield, the C_p at the rotors' surfaces have been plotted, Figure 4.28, for different spanwise locations (70% and 95% of the span) when both rotors overlap, hence, $\Delta\Phi = 0$. This time step has been chosen due to the high aerodynamic interference when the blades are crossing.

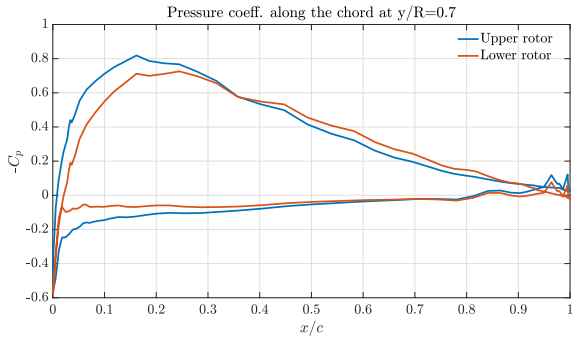

(a) C_p vs x/c at y/R = 0.7

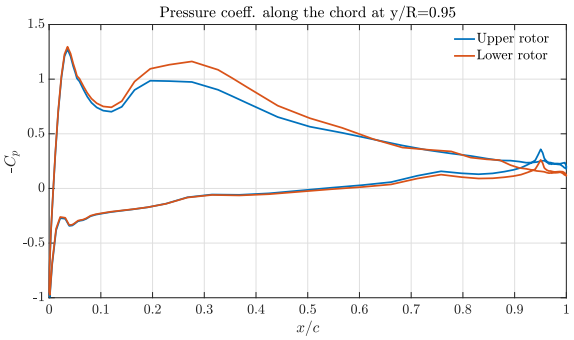

(b) C_p vs x/c at y/R = 0.95

Figure 4.28: C_p in different spanwise slices for the upper and lower rotors, at Φ= 2520º

As previously stated, due to the induced velocity of the upper rotor, the lower one suffers a reduction of the effective angle of attack and, consequently, a reduction of the total thrust. This behaviour is mostly reflected in Figure 4.28a at 70% of the blade span, where the difference of pressure between the upper and lower surface from the lower rotor has decreased with respect to the upper one. Also, as the effective angle has also been reduced, there is a more progressive decrease in pressure and a less intense suction peak. At 95% of the rotor-blade span, in both cases, there is a strong suction peak and a pressure recovery "bubble" where the fluid slows down, as seen for the isolated cases, due to a poor representation of the rotor surface. However, after the slow-down

bubble, a higher acceleration of the fluid is perceived in the lower rotor. This tendency is captured in Figure 4.28b by the upper orange line, but also, when plotting, for both upper and lower rotors, the x-component velocity contour along with pseudo-stream traces for the y/R = 0.95 slice (Figure 4.29). It can be noticed that for the upper rotor, there is a more noticeable boundary layer separation (Figure 4.29a) compared to the lower one (Figure 4.29b), where a thinner recirculation region is captured, due to a higher velocity field around the rotor. This faster inflow velocity is due to the ingestion of the upper rotor wake that produces an acceleration of the flow. In short, despite seeing a higher velocity of the incoming flow for the lower rotor, due to the induced velocity of the upper propeller, the effective angle of attack gets reduced causing a change in its performance and a reduction of the lift coefficient.

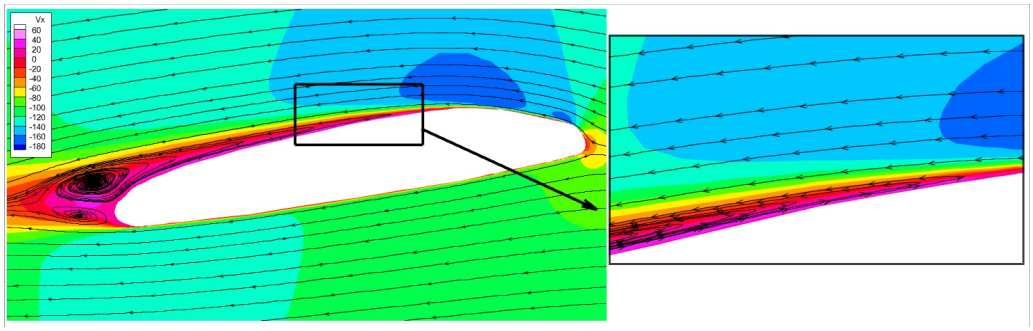

(a) Upper rotor

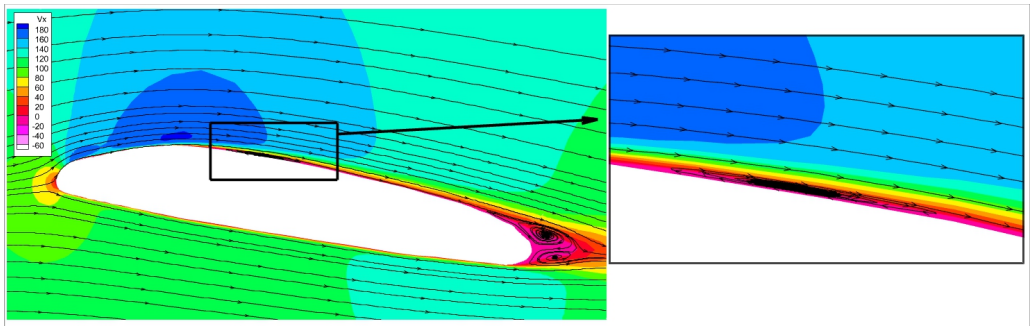

(b) Lower rotor

Figure 4.29: V_x contur and pseudo-streamtraces at y/R = 0.95, at Φ= 2520º

Another way to have a better understanding of the rotor-rotor interference, and determine how the lower blade changes the dynamics of the system, is by studying the shape of the wake region. Figure 4.30 shows, as already done in the isolated cases, a colour map of the V_z along with the pseudo-streamtraces. It is noticeable the presence of strong vortices below the rotors, as a consequence of the recirculation of the flow and the unsteadiness of the first revolutions, hence, more revolutions need to be computed to avoid the interference of those vortices with the wake region. Not working in hovering conditions, and having a

free-stream velocity would have also helped to transport these vortices downstream. The presence of the attached vortices at the centre of the rotor is still noticeable.

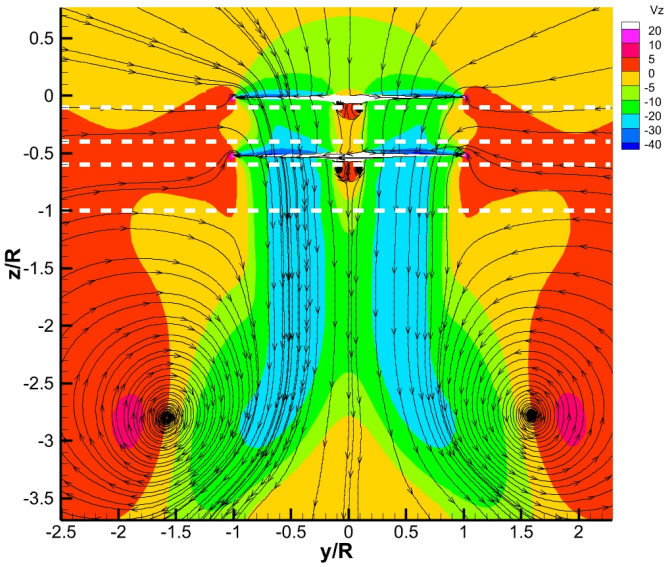

Figure 4.30: V_z contour with pseudo-stream traces for the coaxial case, at Φ= 2520º

Now, having a closer look at the wake shear layer, Figure 4.31 shows a comparison of V_z at different z positions marked as white dashed lines in 4.30; along with, Figure 4.32, that aims to compare the coaxial wake contraction region with the isolated cases.

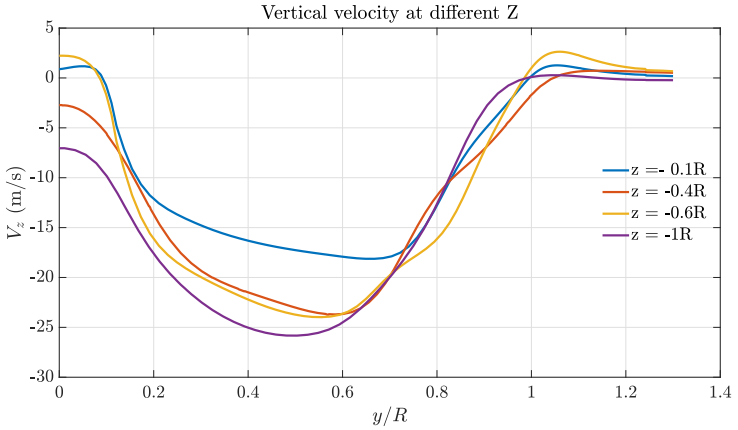

Figure 4.31: V_z trend along radial distance for different z in coaxial, at Φ= 2520º

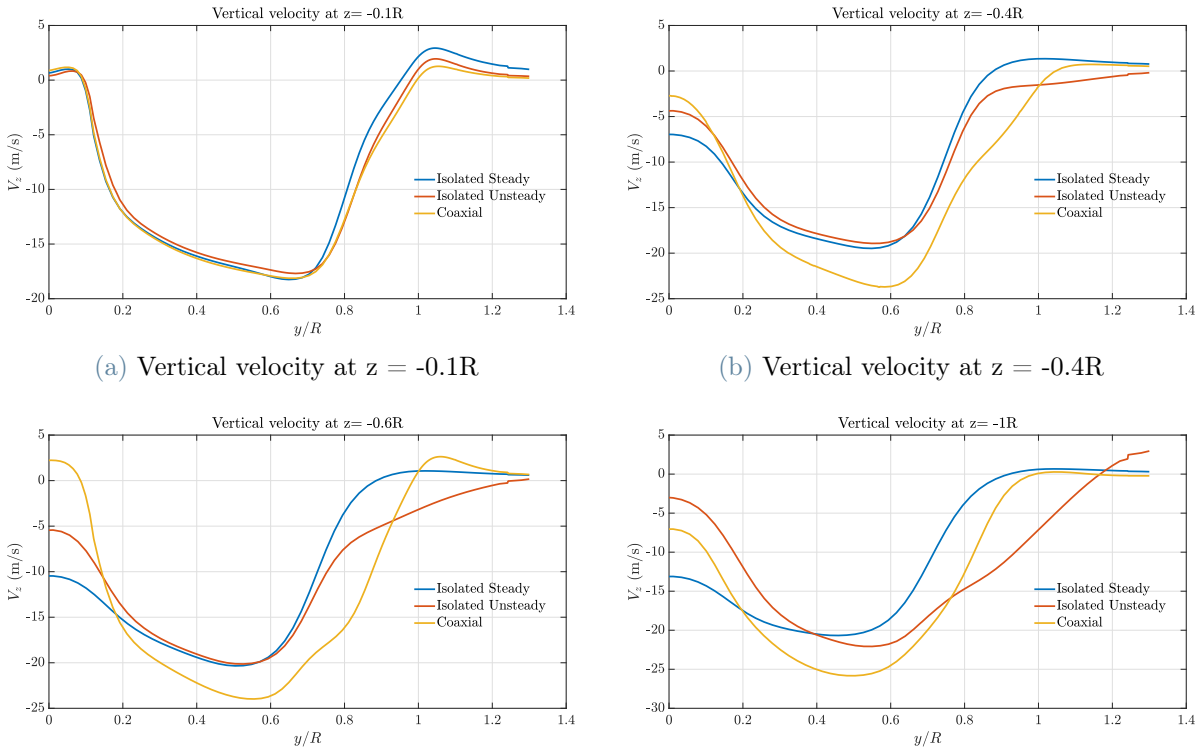

(a) Vertical velocity at z = -0.1R

(b) Vertical velocity at z = -0.4R

(c) Vertical velocity at z = -0.6R

(d) Vertical velocity at z = -1R

Figure 4.32: Comparison of V_z at different z, at Φ_{iso}= 1800º and , at Φ_{coax}= 2520º

At $z = -0.1R$, right after the upper rotor disk, the coaxial configuration shows similar characteristics of the flow field compared to the isolated cases as little influence of the lower rotor is perceived. When approaching the lower rotor, $z = -0.4R$, there is an acceleration of the flow due to the relative motion of the rotor, which creates a suction zone in the upper surface. Once the flow has passed through the second rotor, $z = -0.6R$, more dynamic variations in the shear layer are observed, which are produced by the additional induced velocity of this second rotor. In that region, the actual disk area of the wake for the coaxial rotor is larger than the isolated case. However, far from the rotors, $z = -1R$, the contraction of the wake along with higher velocities is still present for the coaxial case, whereas, the velocity dissipation for the unsteady isolated is more pronounced.

When plotting the contour of the vortex magnitude at the OYZ plane, Figure 4.33, at position $\Phi = 2520^{o}$, hence, $\Delta\Phi = 0^{o}$ between the blades, the wake contraction effect is also captured. There is a clear width reduction of the wake shear layer for both rotors, being the upper wake narrower because of the presence of the lower rotor and its motion. Slightly bigger tip vortices are shed by the lower rotor attributed to the strong vortex-vortex interaction happening at that region, where the vortices coming from the upper rotor are combined with the lower ones, creating more complex structures.

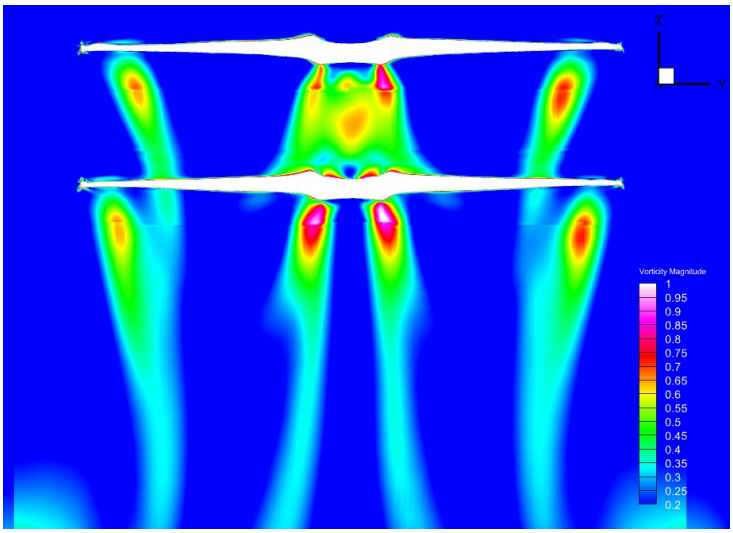

Figure 4.33: Vorticity magnitude visualization, at $\Phi = 2520^{o}$

Another way to visualize the differences between the upper and lower tip vortices is by plotting the iso-surfaces for the q-criterion, Figure 4.34. In this case, there is a difference of $\Delta\Phi = 30\ ^{o}$ between the rotors. The upper vortical structure is more defined compared to the lower one, due to this vortex-vortex interaction. This confirms that the lower rotor wake region dissipates much faster compared to the isolated case.

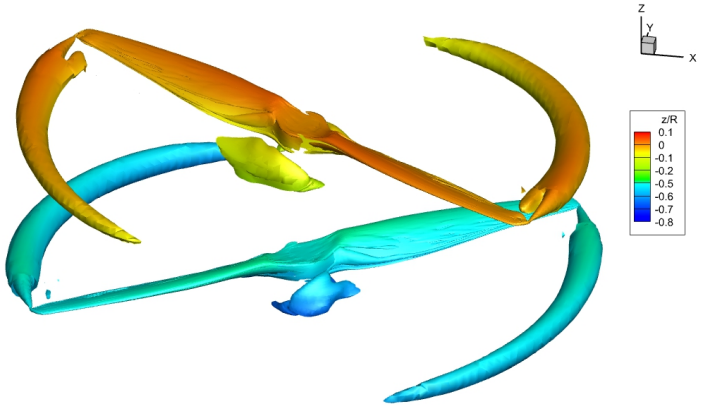

Figure 4.34: ISO-surfaces for the Q-Criterion (Q = 0.2), along with z contour

5 | Conclusions and Future Developments

The aim of this research was to study and understand the flow interaction between coaxial rotors in hover conditions, to effectively apply this knowledge within the eVTOL sector. The in-house ROSITA CFD software has been used to predict the flow field, which is based on the usage of RANS equations together with multi-block structured grids. In order to gain a deeper understanding of the flow dynamics in a coaxial configuration, it has been crucial to examine the isolated rotor and compare its performance with the coaxial one.

As a first approach, results from steady and unsteady isolated simulations have been put in comparison, seeing that for a single rotor, the steady setup is a better choice and gives a slightly better prediction of the flow as it is less complex and time-demanding with respect to the unsteady one. It has been seen that to have a better representation of the flowfield for the unsteady case, more revolutions need to be computed until reaching a periodical behaviour of the loads, and avoid the presence of the detached vortices caused by the initial unsteady motion of the fluid. By plotting different parameters such as the pressure coefficient, velocity contour and pseudo-streamtraces, it has been found that the blade geometry at the blade's tip is causing the fluid in that region to compress and expand, and eventually, come to a boundary layer separation. A smoother surface would have caused a more gradual pressure recovery and a less intense boundary layer separation. Nevertheless, a good representation of the wake contraction right after the rotor has been captured for both steady and unsteady when plotting the vertical velocity in the OYZ plane. Due to the presence of the initial detached vortices for the unsteady case, a more intense dissipation of the wake downstream with respect to the steady setup has been predicted.

Once the performance of the isolated rotor has been studied, the coaxial configuration investigation has been done. As there are two counter-rotating rotors, the simulation must be unsteady, making the total computational cost quite expensive due to the high

total number of elements and the periodical tagging process. It is straightforward that adding a second rotor downstream makes the flowfield change its behaviour. The rotor-rotor interaction has been captured as a pulsation in the aerodynamic loads plot through the revolutions as a consequence of the periodical passage of the blades over each other (4 times per revolution). Moreover, a loss of thrust on the lower rotor compared with the upper one has been observed. This behaviour primarily results from the impact of the downwash from the upper rotor, where the upper-induced velocity causes a reduction of the effective angles of attack of the lower rotor. Additionally, there has been a slight reduction of the upper rotor thrust, in comparison to the isolated case, because of this mutual interaction with the lower rotor. Lastly, when observing the coaxial wake region, a clear compression of the wake shear layer for both rotors has been captured, being the upper wake narrower because of the presence of the lower rotor and its motion. However, less-defined tip vortices are shed by the lower rotor attributed to the strong vortex-vortex interaction happening at that region, where the vortices coming from the upper rotor combined with the lower ones, creating more complex structures.

Additionally, a solid match of ROSITA's result with data from [24] confirms the reliability of code when simulating the aerodynamics of isolated and coaxial rotors.

In conclusion, satisfactory results have been achieved by accurately capturing the rotor-rotor interaction, making this investigation primarily serve as a base for future works.

5.1. Future developments

The initial goal of this research was the aero-acoustic study of this coaxial configuration, however, due to a lack of time it was decided to only proceed with the aerodynamic part. It was intended to use the ROCAAP (ROtorcraft Code for AeroAcoustic Prediction), a code suitable for the study of rotorcraft propagation, which solves the FWH and PS-FWH equations by means of a retarded time algorithm. ROSITA is linked with the acoustics computation as it can generate cylindrical permeable control surface grids by adding the ROSITA.csg and ROSITA.obs files to its directory. As the choice of not doing the acoustic study was a last-minute decision, the acoustic control surfaces were introduced in the different simulation configurations. Figure 5.1 depicts two different control surfaces that will allow a future study of noise generation from the perspective of the rotor's contribution (Figure 5.1b) and the overall system interaction (Figure 5.1a). Hence, the present aerodynamic results and control surface data will serve as a base to compute and study the acoustic of this coaxial configuration and compare the obtained solution with existing noise results in [24]

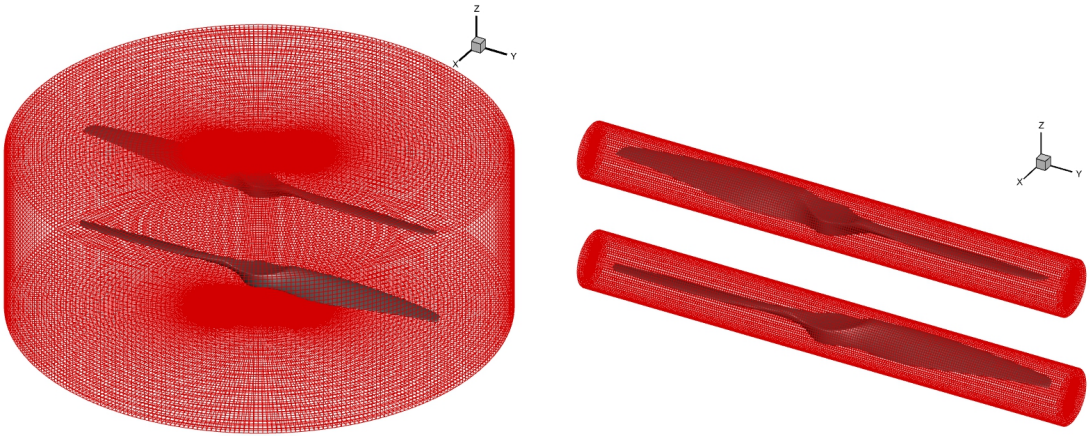

(a) Steady control surface (b) Rotating control surfaces

Figure 5.1: Cylindrical permeable control surfaces

Sticking to the aerodynamics field, in [24], the tandem configuration is also studied, being the distance between the rotors $\Delta z = -0.5R$ and $\Delta x = 2.36D$. Hence, a future analysis of the flow field for a tandem configuration and a comparison with respect to the coaxial setup can be made, by following the same procedures as described in this work, as the meshes were thought to be placed at different positions in the background.

Bibliography

[1] K. Batcher. The architecture of tomorrow's massively parallel computer. *NASA. Goddard Space Flight Center, Frontiers of Massively Parallel Scientific Computation*, 1987.

[2] R. Brown and H. W. Kim. Coaxial rotor performance and wake dynamics in steady and maneuvering flight. In *The American Helicopter Society 62nd Annual Forum, Phoenix, USA, 2006*, 2006.

[3] A. J. Buchner, A. L.-D. ande V. Kitsios, and C.Atkinson. Local topology via the invariants of the velocity gradient tensor within vortex clusters and intense reynolds stress structures in turbulent channel flow. In *Journal of Physics: Conference Series*, volume 708, page 213. IOP Publishing Ltd, 4 2015.

[4] W. Chan, R. Gomez, S. Rogers, and P. Buning. Best practices in overset grid generation. In *32nd AIAA Fluid Dynamics Conference and Exhibit*, page 3191, 2002.

[5] G. Chesshire and W. Henshaw. Composite overlapping meshes for the solution of partial differential equations. *Journal of Computational Physics*, 90(1):1–64, 1990. ISSN 0021-9991.

[6] C. Coleman. A survey of theoretical and experimental coaxial rotor aerodynamic research. *NACA TN 3675*, 3 1997.

[7] P. Concus and G. H. Golub. A generalized conjugate gradient method for nonsymmetric systems of linear equations. In R. Glowinski and J. L. Lions, editors, *Computing Methods in Applied Sciences and Engineering*, pages 56–65, Berlin, Heidelberg, 1976. Springer Berlin Heidelberg.

[8] J. Deng, F. Fan, P. Liu, S. Huang, and Y. Lin. Aerodynamic characteristics of rigid coaxial rotor by wind tunnel test and numerical calculation. *Chinese Journal of Aeronautics*, 32(3):568–576, 2019. ISSN 1000-9361.

[9] W. Gropp, E. Lusk, and A. Skjellum. Using mpi: portable parallel programming with the message-passing interface. *MIT press*, 1, 1999.

[10] R. D. Harrington. Full-scale-tunnel investigation of the static-thrust performance of a coaxial helicopter rotor. *NACA-TN-2318*, 1951.

[11] M. Hilfer and L. Guerra. Boeing autonomous passenger air vehicle completes first flight, 2019. URL `https://boeing.mediaroom.com/2019-01-23-Boeing-Autonomous-Passenger-Air-Vehicle-Completes-First-Flight`.

[12] J. Jeong and F. Hussain. On the identification of a vortex. *Journal of fluid mechanics*, 285:69–94, 1995.

[13] V. K. Lakshminarayan and J. D. Baeder. Computational investigation of microscale coaxial-rotor aerodynamics in hover. *Journal of aircraft*, 47(3):940–955, 2010.

[14] A. J. Landgrebe. The wake geometry of a hovering helicopter rotor and its influence on rotor performance. *Journal of the American Helicopter society*, 17(4):3–15, 1972.

[15] M. Massimo Biava. *ROSITA V4.63 Rotor Software Italy, Formulation and User Manual*. AgustaWestland-Politecnico Advanced Rotorcraft Center s.r.l., Via Durando, 10 - 20158 Milano - Italy, 6 edition, 7 2013.

[16] D. Montagnani, M. Tugnoli, A. Zanotti, M. Syal, and G. Droandi. Analysis of the interactional aerodynamics of the vahana evtol using a medium fidelity open source tool. *VFS Aeromechanics for Advanced Vertical Flight Technical Meeting*, pages 436–451, 2020.

[17] M. Moore. NASA puffin electric tailsitter VTOL concept. In *10th AIAA Aviation Technology, Integration, and Operations (ATIO) Conference*, Reston, Virigina, Sept. 2010. American Institute of Aeronautics and Astronautics.

[18] N. Polaczyk, E. Trombino, P. Wei, and M. Mitici. A review of current technology and research in urban on-demand air mobility applications. In *8th Biennial Autonomous VTOL technical meeting and 6th Annual electric VTOL Symposium*, pages 333–343. Vertical Flight Soc. Mea, Arizona, 2019.

[19] M. Pott-Pollenske and J. Delfs. Enhanced capabilities of the aeroacoustic wind tunnel braunschweig. In *14th AIAA/CEAS Aeroacoustics Conference (29th AIAA Aeroacoustics Conference)*, page 2910, 2008.

[20] A. Straubinger, R. Rothfeld, M. Shamiyeh, K.-D. Büchter, J. Kaiser, and K. O. Plötner. An overview of current research and developments in urban air mobility–setting the scene for uam introduction. *Journal of Air Transport Management*, 87: 101852, 2020.

[21] K. I. Swartz. Charging forward: New evtol concepts advance. *Vertiflite*, 4:24–29, 2017.

[22] A. M. Wissink and R. L. Meakin. On parallel implementations of dynamic overset grid methods. In *Proceedings of the 1997 ACM/IEEE conference on Supercomputing*, pages 1–21, 1997.

[23] S. Xiang, A. Xie, M. Ye, Y. Xufei, X. Han, H. Niu, Q. Li, and H. Huang. Autonomous evtol: A summary of researches and challenges. *Green Energy and Intelligent Transportation*, 3:100140, 11 2023. doi: 10.1016/j.geits.2023.100140.

[24] J. Yin, F. De Gregorio, K.-S. Rossignol, L. Rottmann, G. Ceglia, G. Reboul, G. Barakos, G. Qiao, M. Muth, M. Kessler, A. Visingardi, M. Barbarino, F. Petrosino, A. Zanotti, N. Oberti, L. Galimberti, G. Bernardini, C. Poggi, L. Abergo, F. Caccia, A. Guardone, C. Testa, and S. Zaghi. Acoustic and aerodynamic evaluation of dlr small-scale rotor configurations within garteur ag26. In *49th European Rotorcraft Forum, ERF 2023*, September 2023.

A | Aerodynamic Results

A.1. Steady

A.1.1. 8'000 rpm

- **Convergences Plots:**

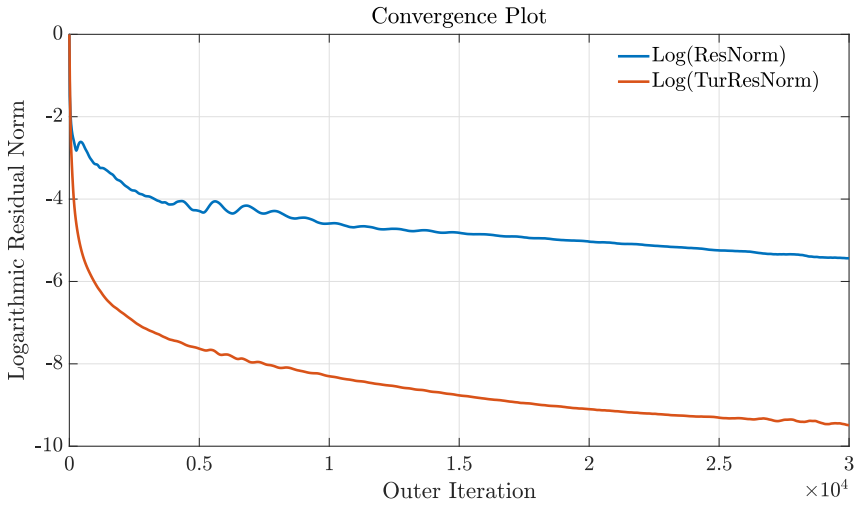

Figure A.1: Residual values for steady isolated-8'000 rpm case

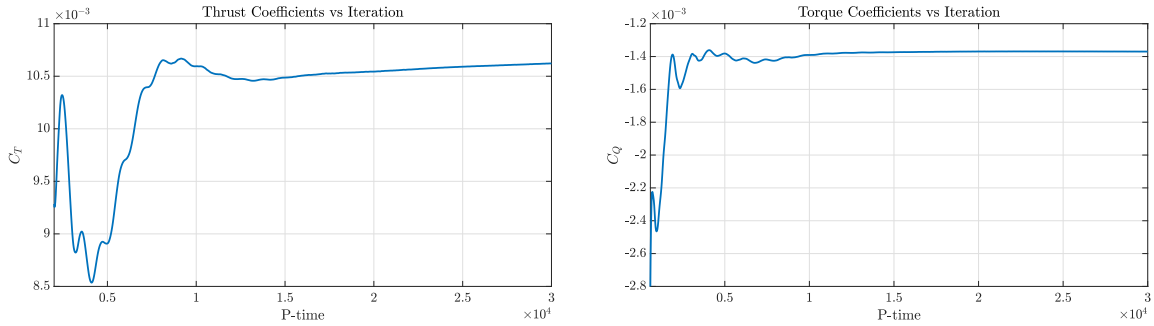

(a) Thrust convergence plot

(b) Torque convergence plot

Figure A.2: Numerical results vs revolutions for steady isolated 8'000 rpm case

A.2. Unsteady Isolated

A.2.1. 8'000 rpm

- **Convergences Plots:**

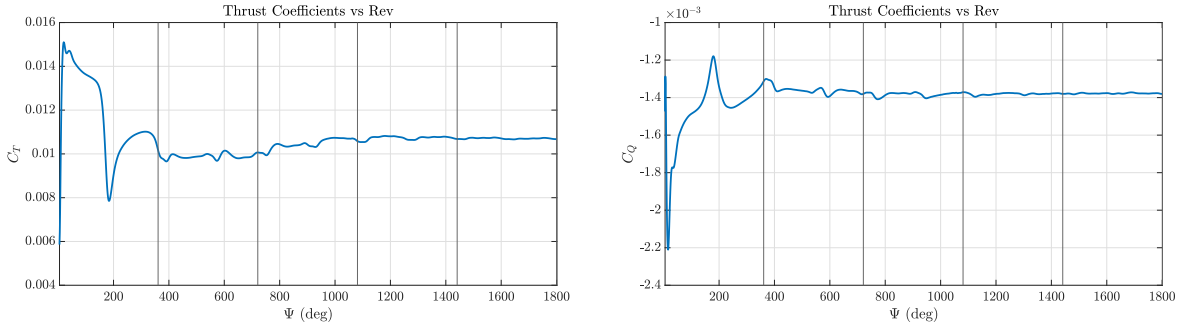

(a) Thrust Coefficients vs Ψ (b) Torque Coefficients vs Ψ

Figure A.3: Numerical results vs revolutions for unsteady isolated-8'000 rpm

A.2.2. 12'000 rpm

- **Convergences Plots:**

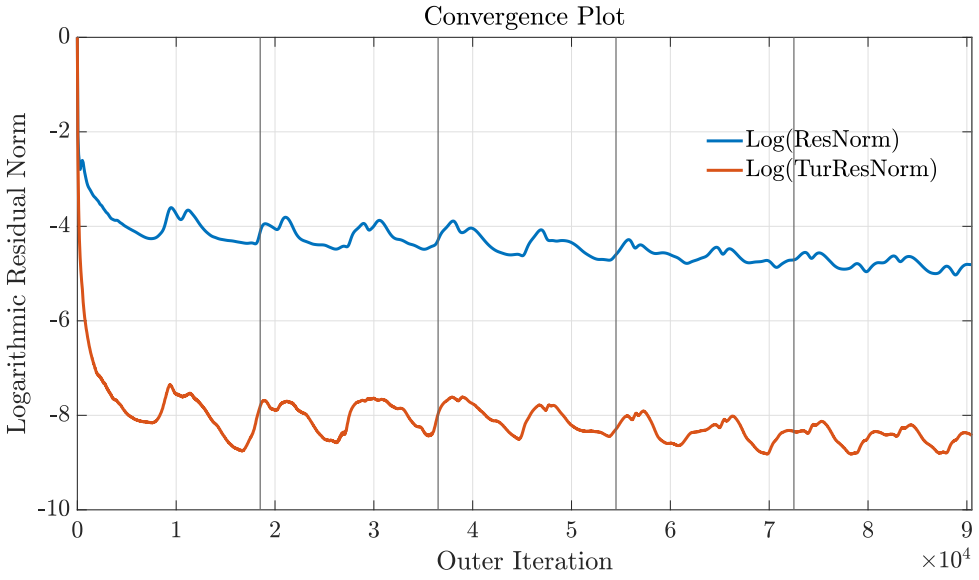

Figure A.4: Residual for unsteady isolated-12'000 rpm case

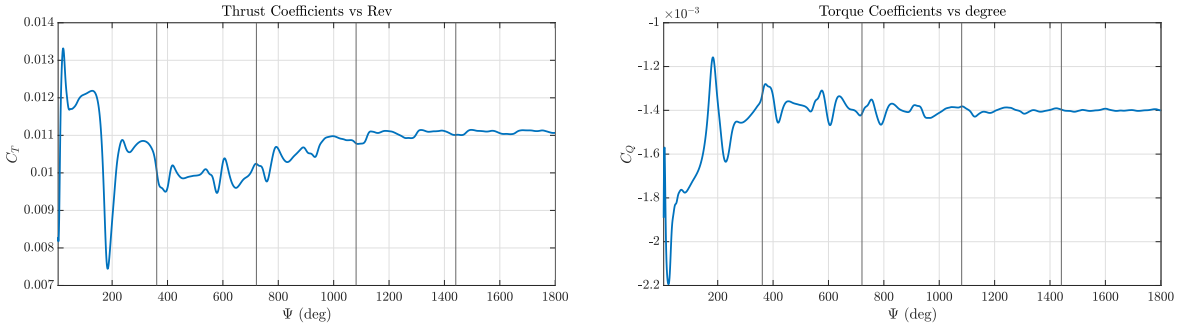

(a) Thrust Coefficients vs Ψ (deg) (b) Torque Coefficients vs Ψ (deg)

Figure A.5: Numerical results vs revolutions for unsteady isolated-12'000 rpm

A.3. Coaxial

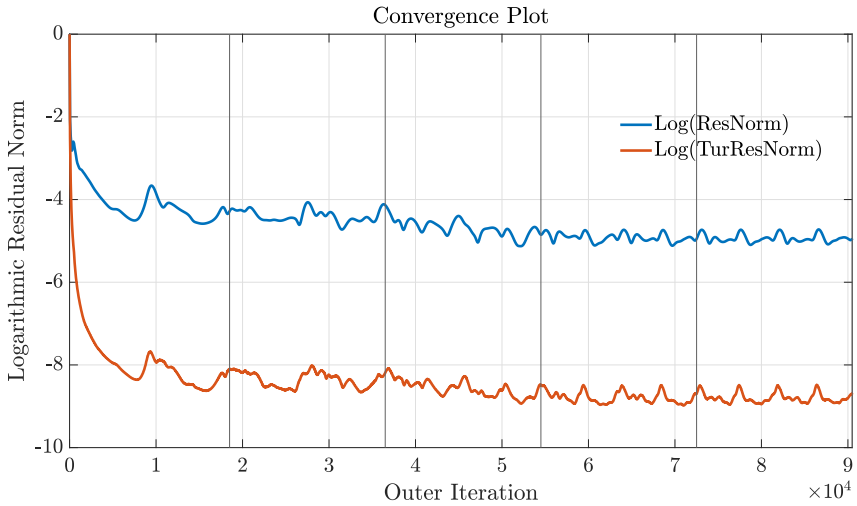

Figure A.6: Residual for the coaxial 8'000 rpm case

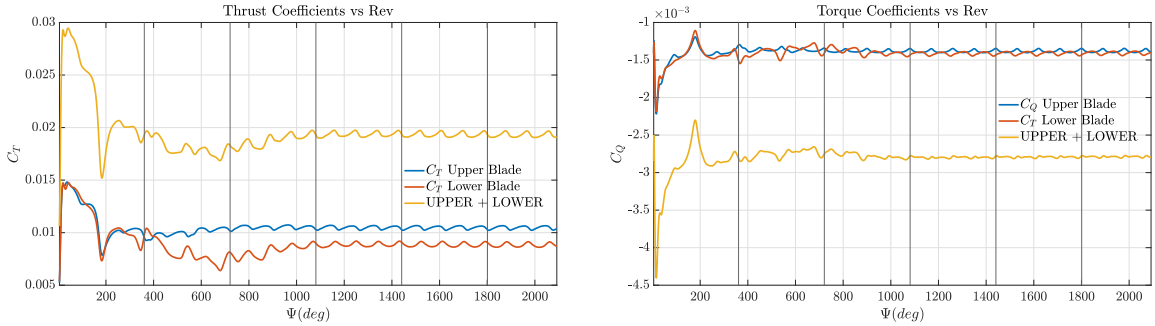

(a) Thrust Coefficients vs Ψ (deg) (b) Torque Coefficients vs Ψ (deg)

Figure A.7: C_T and C_Q for upper and lower rotors along with its sum

List of Figures

List of Tables

List of Symbols

Variable	Description	SI unit
$\boldsymbol{T}$	Thrust	N
$\boldsymbol{T_{ref}}$	Reference thrust	N
$\boldsymbol{C_T}$	Thrust coefficient	
$\boldsymbol{M_z}$	Torque	Nm
$\boldsymbol{Mz_{ref}}$	Reference torque	N
$\boldsymbol{C_Q}$	Torque coefficient	
$\boldsymbol{C_P}$	Pressure coefficient	
$\boldsymbol{\rho_\infty}$	Free stream density	kg/m^3
$\boldsymbol{P_\infty}$	Free stream pressure	Pa
$\boldsymbol{c_\infty}$	Free stream speed of sound	m/s
$\boldsymbol{l_{ref}}$	Rotor radius	m
$\boldsymbol{u}$	fluid velocity	m/s
$\boldsymbol{\omega_{dim}}$	Dimensional angular velocity	rad/s
$\boldsymbol{t_{dim}}$	Dimensional time	s
$\boldsymbol{P_{dim}}$	Dimensional pressure	Pa
$\boldsymbol{F_{dim}}$	Dimensional force	N
$\boldsymbol{\Theta}$	Geometric blade twist	º
$\boldsymbol{t}$	Blade thickness	m
$\boldsymbol{c}$	Blade chord	m
$\boldsymbol{M_{tip}}$	Blade tip Mach number	
$\boldsymbol{RPM}$	Revolutions per minute	1/min
$\boldsymbol{r}$	Cylinder grid's radius	m
$\boldsymbol{L}$	Cylinder grid's length	m
$\boldsymbol{y^+}$	Non-dimensional wall distance	

Variable	Description	SI unit
$\boldsymbol{\Phi}$	Azimuthal angle	º
$\boldsymbol{F_{nz}}$	Normal z-component force	N
$\boldsymbol{F_{tz}}$	Tangential z-component force	N
$\boldsymbol{M_{nz}}$	Normal z-component moment	Nm
$\boldsymbol{M_{tz}}$	Tangential z-component moment	Nm
$\boldsymbol{V_{tip}}$	Rotor's tip velocity	m/s
$\boldsymbol{R}$	Rotor's radius	m
$\boldsymbol{D}$	Rotor's diameter	m
$\boldsymbol{\gamma}$	Heat capacity ratio	
$\boldsymbol{V_z}$	Vertical velocity	m/s
$\boldsymbol{\nabla_v}$	velocity gradient tensor	s^-1
$\boldsymbol{S}$	Strain tensor	s^-1
$\boldsymbol{\Omega}$	Rotational tensor	s^-1
$\boldsymbol{D}$	First invariant of $\boldsymbol{\nabla u}$	s^-1
$\boldsymbol{Q}$	Second invariant of $\boldsymbol{\nabla u}$	s^-1
$\boldsymbol{R}$	Third invariant of $\boldsymbol{\nabla u}$	s^-1

Acknowledgements

And with this research, a long chapter of my life has been closed. Ending my academic journey with the elaboration of this project has been a very rewarding challenge. Firstly, I would like to express my gratitude to Prof. Luigi Vigevano for motivating me to do this research and for his support during the process, not without mentioning the great assistance of Yi Yuan and his availability during the work.

Coming from another country with different teaching methods and a slightly diverse culture has meant an excellent learning opportunity, both academically and personally. Therefore, I want to thank all those people who have stood by my side during this journey.

Firstly, I want to thank my family, especially my mum and dad. Without them, I wouldn't have been able to come to study this master's degree in Italy, both for the financial and emotional support. From a very young age, they have taught me that with perseverance, discipline, and motivation, one can reach whatever one wants, and this has been key to my personal and academic achievements. Thank Mom, for supporting me through my highs and lows, and for listening to me and giving me advice when I needed it most. Thank you, Dad, for helping me disconnect from academic life by taking me to the mountains or by the sea to do all kinds of sports, while also teaching me to be responsible for my duties and knowing when to be hard-working or to relax.

A heartfelt thank you to my dear friends, without whom these past two years wouldn't have been the same. Nil, you've been the reason I'm writing this now. Who would have thought back in Terrassa, in our first years of university, that we would end up here in Milano together? You have undoubtedly been my most fundamental person, being by my side during the good and bad times. To my flatmates, Daniel and Juan. Having lived with you has made everything much easier, you do not know how grateful I am to have such good memories with you two. I am convinced that this friendship will last long.

To conclude, I want to thank all my Italian friends who have introduced me to the Italian culture and welcomed me with open arms even when I didn't speak Italian. Especially to Matteo, Giacomo, and Felice, who have made me feel at home since day one.